Supplementary Materials for

Adrenergic nerves activate an angio-metabolic switch in prostate cancer

Ali H. Zahalka, Anna Arnal-Estapé, Maria Maryanovich, Fumio Nakahara, Cristian D. Cruz, Lydia W. S. Finley, and Paul S. Frenette

correspondence to: paul.frenette@einstein.yu.edu

This file includes:

Materials and Methods

Animals and *in vivo procedures*

B6.Cg-Tg(Cspg4-cre/Esr1*)BAkik, *Adrb2*^{tm1Bkk}, *Adrb3*^{tm1Lowl}, *Cox10*^{tm1Ctm} (all from Jackson Laboratory); C57BL/6 Charles Rivers; BALB/c nude (from Charles Rivers and Taconic); FVB-Tg(ARR2/Pbsn-MYC)7Key (from the National Cancer Institute); *Adrb2*$^{fl/fl}$ mice were a kind gift from G. Karsenty; *Cdh5-Cre*^{ERT2} mice were a kind gift from R.H. Adams; *Csf1r-iCre* mice were a kind gift from J.W. Pollard.

All *in vivo* experiments were approved by the Animal Care and Use Committees of the Albert Einstein College of Medicine. Orthotopic human PC3-luciferase tumors were implanted into 6- to 8-week-old male mice, and monitored by bioluminescence imaging as previously described (*9*). *In vivo* fluorescence imaging of angiosense vascular pooling agent (PerkinElmer) was performed by intravascular injection of the agent and analyzed 24 h later using an IVIS imaging system 200 series (PerkinElmer).

Orthotopic co-transplantation of culture-expanded prostate endothelial cells (Angiocrine Bioscience) and prostate tumor cells was performed by co-injection of 10^5 GFP-tagged endothelial cells and 5 x 10^4 PC-3 cells suspended in 20µL endothelial cell media (*Cell Culture* below) containing 5% growth factor reduced (GFR) Matrigel (Corning) into the ventral prostates of 6- to 8-week-old male mice. Animals were sacrificed two weeks after transplantation, and the tumors removed for analysis.

To assess vascular recruitment *in vivo* in immune-competent mice, pure type I collagen matrices (Advanced BioMatrix), were cut in half along their diameter and then carefully inserted in-between the two ventral prostate lobes through a 2.5 mm incision made in the prostate capsule using fine iris scissors (paying close attention to avoid damaging the prostate lobes). Animals were sacrificed four weeks after transplantation and the ventral prostates removed for imaging.

Chemical sympathectomy (adrenergic denervation) was performed by intraperitoneal injection of 6OHDA (Sigma), given at a first dose of 100mg/kg (freshly dissolved in PBS prior to injection, to minimize oxidation), and a second dose of 250 mg/kg 72h later. For *Cre*^{ERTM} and *Cre*^{ERT2} mediated recombination, 2mg tamoxifen (Sigma) was administered by intraperitoneal injection, once daily for five consecutive days.

To assess prostate perfusion, mice were injected IV with 126mg/kg luciferin (Goldbio) dissolved in sterile saline, which was allowed to circulate for 1 minute. Mice were then immediately sacrificed, 500µL of blood was removed by intracardiac puncture and placed in Eppendorf tubes containing 20µL EDTA, and prostates were removed and dissected on ice. Prostates were then minced with scissors and digested for 30 minutes at 37°C in digestion buffer (see *Cell Sorting and Flow Cytometry* section), and then centrifuged for 4 minutes to pellet the cells. The supernatant was removed and saved for analysis. Blood was centrifuged at 1200 x g for 15 minutes to isolate plasma (this served as the internal control). Luciferin content was measured by addition of the luciferase enzyme with excess ATP (so that sample luciferin content would be the limiting factor in light generation; Promega) and luminosity recorded with a luminometer (Perkin Elmer). Prostate luminescence was normalized to plasma luminescence and then expressed as relative luminescence units (RLU) / mg tissue weight.

Immunohistochemistry and histology

Preparation of tumor, prostate, and orthotopic matrix frozen sections: tissues were perfusion-fixed, then post-fixed in 4% paraformaldehyde overnight at 4°C, then incubated in 15% sucrose and 30% sucrose for cryoprotection, then embedded in OCT cryomedium (Tissue-Tek) and flash-frozen in 2-methylbutane (Sigma) cooled in liquid nitrogen. Tissues were warmed to -20°C, trimmed to full face,

and sectioned at 100μm (thick sections) or 20μm (thin sections) using high-profile cryotome blades (Sakura Finetek).

Immunofluorescence staining of thick tissue sections: slides were blocked/ permeabilized in PBS containing 20% normal donkey serum (Sigma) and 1% Triton X-100 for 45mins at room temperature. Slides were incubated with primary antibody in 5% normal donkey serum with 0.01% Triton X-100 overnight at 4°C. Secondary antibody was applied for 45 min at room temperature.

Immunofluorescence images were acquired with an AXIO Examiner D1 microscope (Zeiss), equipped with a confocal scanner unit CSU-X1 (Yakagawa), and automated micrometer stage (Sutter Instrument). Z-stack montage images were stitched together and reconstructed in SlideBook software (Intelligent Imaging Innovations). For quantification of vascular indices of angiogenesis, images were analyzed using the Simple Neurite Tracer plug-in (*12*) found in the Fiji build of ImageJ (NIH). To quantify the proximity of interaction between adrenergic nerves and the vasculature we employed a combination of morphometry and proximity analysis that has been used for studying neural organization in the central nervous system (*44*). Briefly, all vessels and nerves in an image were traced using Simple Neurite Tracer and converted into skeleton representations. The SWC skeleton files were then imported into the statistical programming language R, and all nerves and all vessels were converted into point vector representations with the dotprops function of the NBLAST package (*45*), and proximity of interaction calculated using the neuriteblast function of the same package, using a σ of 10μm. The average of the forward and reverse interaction for each nerve – vessel pair was calculated and then weighted based upon the vessel's length as a percent of total vessel coverage in the image. Thus, the proximity scores range from 0 to 1, where 0 = complete overlap, 0.5 = close association of two structures, and 1 = no association.

For pathology analyses, paraffin-embedded prostate tissues were trimmed to full-face then sectioned at 5 μm thickness and stained with hematoxylin and eosin. Entire cross-sectional images of slides were acquired with the P250 High Capacity Slide Scanner (PerkinElmer) and pathology manually analyzed (all lobes excluding coagulation glands) in Panoramic Viewer (3dhistotech).

To assess vascular leakage, 70,000 MW Texas Red-conjugated dextran was injected IV and allowed to circulate for 30 minutes. Tissues were then perfused, fixed, and processed. Vascular leakage was assessed by quantifying relative dextran fluorescence in the prostate interstitium.

For COA6 quantification, equal amounts of protein from cell lysates were subjected to SDS-PAGE, followed by western blot analysis using anti-β-actin and anti-COA6 antibodies (see *Antibodies and Staining Reagents* below).

Catecholamine measurement

Prostates were freshly dissected and immediately flash frozen in liquid nitrogen. Tissue samples were homogenized in 0.1M tricholoroacetic acid containing 10^{-2}M sodium acetate, 10^{-4}M EDTA, 5ng/mL isoproterenol (as an internal standard) and 10.5% methanol (pH 3.8), and centrifuged at 10,000 x g for 20 minutes, and the supernatant was analyzed by high pressure liquid chromatography (HPLC) by the Neurochemistry Core Laboratory at Vanderbilt University's Center for Molecular Neuroscience Research (Nashville, TN).

Cell sorting and flow cytometry

Endothelial cells were isolated from dissected prostate and tumor tissues by mincing tissues in digestion buffer composed of Hank's balanced salt solution (HBSS; Gibco), 2.5 mg/mL collagenase IA (Sigma), 0.6 mg/mL dispase (Gibco), 0.25 mg/mL DNase I (Sigma), 20mM HEPES (Gibco), and incubated at 37°C for 35 min on a rotating rack. All cell sorting experiments were carried out using an Aria Cell Sorter (BD Biosciences), and all flow cytometric analyses were carried out using an LSRII

flow cytometer running FACS Diva 8.0 software (all BD Biosciences). Samples were run in azide-free FACS buffer (so as to avoid mitochondrial damage), and cell doublets, debris, and dead cells were excluded by FCS, SSC, and DAPI (4',6-diamidino-2-phenylindole) profiles. Data were analyzed by FlowJo (Tree Star) software.

To assess endothelial mitochondrial membrane potential $\Delta\psi$, cell suspensions were stained on ice with cell surface markers (*Antibodies and Staining Reagents* below), then incubated in 100 nM TMRE (life technologies) with 50 nM Mitotracker green or Mitotracker deep red (Life Technologies and Cell Signaling Technologies, respectively) in HBSS containing 40 μM verapamil (to inhibit cell surface P-glycoprotein efflux pumps from expelling TMRE; Sigma) for 20 min light-protected at 37°C. TMRE and Mitotracker green (or deep red) fluorescence were determined by flow cytometry.

To assess endothelial glucose uptake, cell suspensions were stained on ice with cell surface markers (*Antibodies and Staining Reagents* below), then incubated in 100 μM of the fluorescent deoxyglucose analog 2-NBDG (Cayman Chemical) suspended in glucose-free, pyruvate-free, glutamate-free Dulbecco's Modified Eagle Medium supplemented with 1x GlutaMAX (both from ThermoFisher Scientific). 2-NBDG fluorescence was quantified by flow cytometry.

To assess endothelial NADH levels, cell suspensions were stained on ice with cell surface markers (*Antibodies and Staining Reagents* below), then stained with the fixable viability dye eFluor 506 (eBioscience) in HBSS for 25 minutes. Since NADH exhibits a characteristic autofluorescent peak at 470nm after excitation by a UV laser *(27)*, mitochondrial NADH was calculated as a ratio of basal NADH autofluorescence in half the sample, then maximal NADH after addition of 2 μg of antimycin A (Sigma), a potent inhibitor of oxidative phosphorylation, in the other half. To assess endothelial cell respiratory capacity (RC), cell suspensions were prepared as described above, then basal oxidized NAD^+ levels (the non-autofluorescent fraction) were measured in half the sample, then maximal levels after addition of 1μM of the oxidative phosphorylation uncoupler FCCP (Cayman Chemical), thus achieving maximal respiration. RC was calculated as a ratio of maximal NAD^+ levels to basal levels.

To assess cell proliferation and apoptosis by flow cytometry, cells suspensions were stained on ice with cell surface markers (*Antibodies and Staining Reagents* below), then with the fixable viability dye eFluor 506, followed by cell fixation and permeabilization and stained with the primary antibodies to Ki-67 (for proliferation) and cleaved CASP3 (for apoptosis; see *Antibodies and Staining Reagents* below) according to the manufacturer's instructions (BD biosciences). After exclusion of dead cells (by eFluor 506 fixable viability dye), Ki-67 and cleaved CASP3 fluorescence was measured by flow cytometry.

Antibodies and staining reagents

Alexa Fluor 647-anti-CD31 (MEC13.3), Alexa Fluor 700-anti-CD45 (30-F11), Alexa Fluor 700-anti-TER119 (TER-119), Alexa Fluor 700-anti-Ly6A/E (D7), PE-Cy7-anti-CD117 (2B8) [all Biolegend]; PerCP-eFluor 710-anti-Ki-67 (SolA15), PerCP-Cy5.5-anti-CD11b (M1/70), PE-anti-PDGFRα (APA5), APC-anti-PDGFRβ (APB5), APC/APC-eFluor780/FITC-anti-EpCAM (G8.8), PE-Cy7-anti-CD31 (390), Alexa Fluor 488/eFluor660-anti-Lyve-1 (ALY7), Streptavidin APC-eFluor 780 [all eBioscience]; FITC-anti-Active cleaved Caspase-3 (C92-605), Biotin-anti-Lineage panel cocktail [TER-119 (TER-119), Ly-6G/C (RB6-8C5), CD11b (M1/70), CD3e (145-2C11)] [BD Bioscience]; anti-C1orf31 (COA6) [Protein Biotechnologies]; Alexa Fluor 488/568/647-anti-rabbit, and Alexa Fluor 594 Cick-iT® Plus TUNEL [Thermo Fisher]; anti-tyrosine hydroxylase, anti-NG2, Alexa Fluor 555 anti-α-tubulin [Millipore]; Cy3-anti-αSMA antibody, anti-β-actin, and Hoechst 33342 [Sigma].

Cell culture and *in vitro* assays

PC-3 cells stably expressing luciferase (luciferase construct, gift from W. Guo, Albert Einstein College of Medicine) were cultured in Ham's F-12 Nutrient Mix (Gibco), supplemented with 10% FBS (Gibco), 1.5 g/L sodium bicarbonate (Sigma), and 500 mg/mL G418 (Sigma).

Culture-expanded primary mouse prostate endothelial cells (Angiocrine Biosciences) were plated on 2μg/mL fibronectin-coated culture dishes and cultured according to the manufacturer's protocol. To selectively knockdown *Adrb2* in VeraVec prostate endothelial cells, *Adrb2*/Control short hairpin RNA (shRNA) lentiviruses were generated by co-transfecting HEK-293T cells with 12μg shRNA shuttle vector (GIPZ Lentiviral shRNA Library, OpenBiosystems, provided by John F. Reidhaar-Olson at the Einstein shRNA Facility), 0.6μg tat vector, 0.6μg gag/pol vector, 1μg vsv-g vector using 45μL TransIT-X2 transfection reagent (Mirus Bio). Supernatant was collected from transfected HEK cells, filtered, and concentrated by ultracentrifugation. Concentrated virus preparations were used to transduce prostate endothelial cells, and cells expressing the construct (expressing GFP) were selected by FACS sorting. To selectively overexpress *Coa6*/*Bckdha*/or Control-GFP in VeraVec prostate endothelial cells, lentivirus vectors were made by cloning *Coa6* or *Bckdha* gene from pCMV-SPORT6 vectors (OpenBiosystems Library provided by John F. Reidhaar-Olson at the Einstein shRNA Facility) into pHIV-IRES-ZsGreen vector (a kind gift from Chan-Jung Chang, Mount Sinai School of Medicine) using Gateway cloning System (Thermo Fisher Scientific). Then lentiviruses were generated by transfecting 12mg of pHIV/ Coa6, Bckdha or empty control vector with 0.6μg tat vector, 0.6μg rev vector, 0.6μg gag/pol vector, and 1μg vsv-g vector using 45μl TransIT-X2 transfection reagent (Mirus Bio). Supernatant was collected from transfected HEK cells, filtered, and concentrated by ultracentrifugation.

To measure endothelial cell migration, cells were plated on fibronectin-coated culture dishes and allowed to reach confluence. Complete media was then replaced with serum free, cytokine-free media and cells were allowed to acclimate for 4 h at 37˚C, before a "scratch" was created in the confluent monolayer with a p200 pipette tip. Images were acquired after the scratch was made (time 0) and imaged again 36 hours later. Migration was calculated as the percentage of the scratch area covered by migrating cells 36 h post scratch, and then normalized to control. cAMP levels were measured using a cAMP ELISA Kit according to the manufacturer's instructions (Cell Biolabs, Inc.) after cells were stimulated for 30 minutes with 10μM noradrenaline (the adrenergic neurotransmitter) in the presence of 0.5mM of the phosphodiesterase inhibitor IMBX (3-isobutyl-1-methylxanthine; Sigma). For adenylyl cyclase experiments, cells were incubated for 36 h prior to analysis with either 10μM forskolin (Cayman) or 300μM SQ 22,536 (Cayman) in the presence of 10μM noradrenaline.

Metabolic assays

For all metabolic experiments, endothelial cells were re-suspended in serum-free media containing 5mM glucose and 5% GFR Matrigel 36 h prior to analysis. For experiments involving shAdrb2 or βAdR^{KO}-derived endothelial cells, GFR-containing media was supplemented with 10μM noradrenaline (the adrenergic neurotransmitter) and 100μM ascorbic acid (to prevent noradrenaline oxidation; both from Sigma). For galactose experiments, cells were seeded in 5mM glucose-containing media and the next day media was either replaced with fresh 5mM glucose (Sigma)-containing media or 5mM galactose (Sigma)-containing media. ATP levels were measured in lysed endothelial cells using the ATPlite Luminescent kit (PerkinElmer) according to the manufacturer's instructions. Lactate concentration was measured in cell supernatant using the Lactate Assay Kit (BioVision) according to the manufacturer's instructions, and levels normalized to total protein content in each sample and then displayed relative to control.

Endothelial respiration (oxygen consumption rate) was measured using the XFe96 analyzer (Seahorse Bioscience). For shAdrb2 and Coa6-GFP experiments, $3.5x10^4$ cells were added per well in

XFe96 microplates. βAdR^{KO} and βAdR^{WT} -derived endothelial cells were obtained by FACS sorting 10^4 endothelial cells, freshly isolated from day 18 tumors (including the surrounding prostate tissue), directly into the center of each well in XFe96 microplates. Matrigel-containing media was replaced 1 h prior to the assay with non-buffered assay medium supplemented with 20% KnockOut Serum Replacement (ThermoFisher Scientific) and placed in a carbon-dioxide-free incubator. Oxygen consumption rate was measured sequentially under basal conditions, in response to 3μM oligomycin (an ATP synthase inhibitor), 1μM FCCP (a mitochondrial uncoupler), and 4μg/mL of antimycin A with 3μM rotenone (both potent inhibitors of oxidative phosphorylation).

To perform metabolite profiling and isotope tracing, cells were seeded on fibronectin-coated 6-well plates dishes in pyruvate-free, glucose-free, glutamine-free DMEM, supplemented with 5mM ^{12}C-glucose (Sigma), 2mM ^{12}C-glutamine (Gibco), or their uniformly labeled ^{13}C counterparts [U-^{13}C]-glucose and [U-^{13}C]-glutamine (Cambridge Isotope Laboratories), and 20% KnockOut Serum Replacement. Media was changed at the indicated time before analysis. Metabolites were extracted in 80% methanol containing 20μM of deuterated 2-hydroxyglutarate (d5-2HG) as an internal standard, and processed as previously described (*46*). To derivatize metabolites, they were methoximated and trimethylsilylated as previously described (*46, 47*). Metabolite profiles were analyzed by gas chromatography mass spectrometry under electron impact ionization using an Agilent 7890A GC coupled to an Agilent 5975C mass selective detector (Agilent Technologies) and peaks representing metabolites of interest were extracted and integrated using MassHunter software (Agilent). Values were then normalized to the internal standard, d5-2HG, and to duplicate sample protein content. Natural isotope abundance correction was performed by IsoCor software (*48*). Samples for liquid chromatography mass spectrometry (LC-MS) metabolite profiling were diluted with 10mmol ammonium acetate in methanol, containing acyl carnitine stable isotope standards (d_3-C0, d_3-C2, d_3-C3, d_3-C4, d_3-C5, d_3-C6, d_3-C8, d_3-C10, d_3-C12, d_3-C14, d_3-C16, d_3-C18), lipid internal standards (lysoPC a C9:0, PC aa C28:0, PC aa C40:0, SM C6:0), and injected into LC-MS for flow injection analysis.

Microarray and Gene Set Enrichment Analysis

Total RNA from sorted endothelial cells was extracted using RNeasy Plus Micro Kit (Qiagen) according to the manufacturer's instructions, and quality verified using the Agilent Bioanalyzer (Agilent Technologies). All further steps were performed at the Genomics Core Facility at the Albert Einstein College of Medicine according to the appropriate Affymetrix protocols, including RNA labelling with the GeneChip wild-type terminal labelling kit (Affymetrix), hybridization to Mouse Gene 2.0 ST arrays, and scanned. Raw data was normalized using the RMA algorithm in the Expression Console Software (Affymetrix), and unsupervised hierarchical clustering of genes that exhibited a $\geq$ 1.6-fold change in expression and an ANOVA p-value < 0.05, was performed in the Transcriptome Analysis Console Software (Affymetrix). Gene set enrichment analysis (GSEA) was performed with C5 gene sets from the Molecular Signatures Database 5.0 (Broad Institute).

RNA extraction and qRT-PCR

mRNA was extracted and purified from cells sorted into lysis buffer (LifeTechnologies) using the Dynabeads mRNA DIRECT purification kit (LifeTechnologies), and reverse-transcribed using the RNA to cDNA EcoDry Premix (Clonetech), according to the manufacturer's instructions. Quantitative PCR (qPCR) was performed either with SYBR GREEN master mix (primer sequences below; Roche), or TaqMan Gene Expression Master Mix (TaqMan Gene Expression Assays below; Applied Biosystems), and run on a QuantStudio 6 Real-Time PCR System (Applied Biosystems). The average threshold cycle number (Ct) for each tested gene was used to quantify relative expression: $2^{-(Ct(gene) - Ct(control))}$. Primers sequences include: *Gapdh* forward, TGTGTCCGTCGTGGATCTGA; *Gapdh* reverse, CCTGCTTCACCACCTTCTTGA; *Adrb2* forward, ATCTGAAGGAAGATTCCACGCCCA; *Adrb2*

reverse, AGAGGGTGAATGTGCCCATGATGA. TaqMan Gene Expression Assays include: *Coa6* Mm00612966_m1; *Bckdha* Mm00476112_m1; *Fh1* Mm01321349_m1; *Gapdh* Mm99999915_g1.

Statistical analysis

All data are represented as mean ± s.e.m., except for seahorse OCR plots that are represented as mean ± s.d. Comparison between two samples was performed using un-paired two-tailed Student's *t* test. Comparison between multiple groups was performed using one-way ANOVA followed by Tukey's multiple comparison test. Comparison between seahorse OCR plots was performed using a two-way ANOVA followed by Bonferroni's multiple comparison test. Statistical analysis was performed with Prism 7 software (GraphPad).

Supplementary Figures:

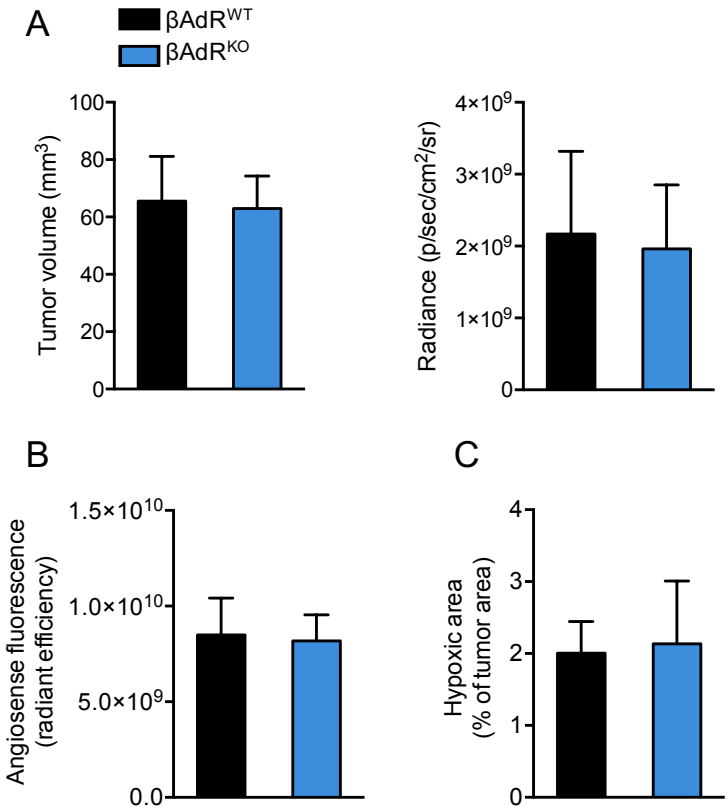

Fig. S1. Pre-angiogenic switch (+18 days) βAdR^{KO} and βAdR^{WT} tumors display similarities in size and vascular function. (**A**) Quantification of tumor volume (using formula, volume = 0.5 length x width^2; left), and luminescence by IVIS 18 days post tumor implantation (right). (**B**) Tumor vascular leakage assessed by *in vivo* angiosense fluorescence 24 h after injection. (**C**) Tumor hypoxia assessed in tumor cross-sections by pimonidazole positive areas. All experiments n = 4 mice/condition. Error bars = s.e.m. All *p*-values were not significant (> 0.05).

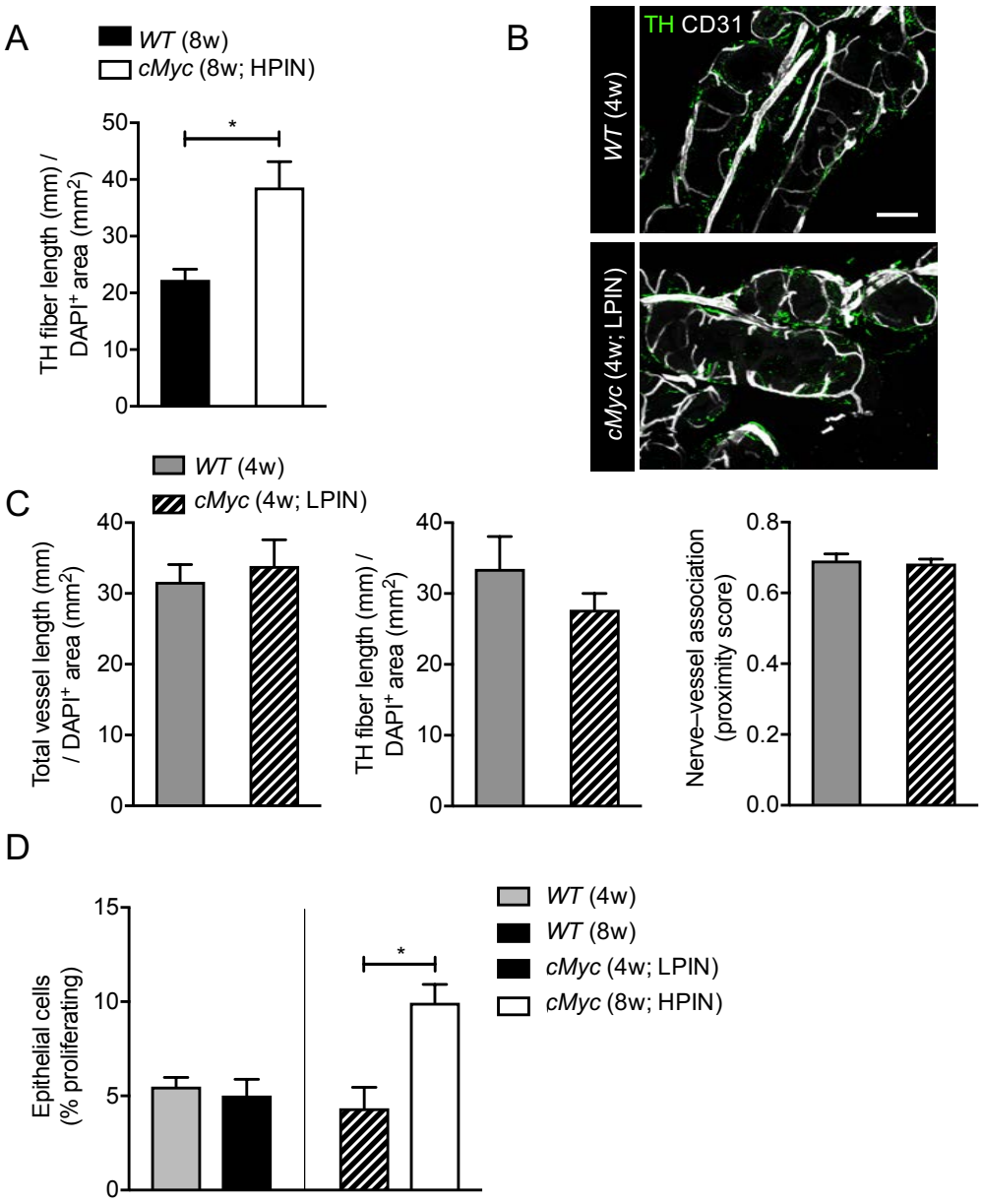

Fig. S2. Minimal adrenergic nerve – vessel interaction is observed in the pre-neoplastic LPIN stage. (**A**) Quantification of adrenergic nerve density in the HPIN stage. n = 4 mice/condition. (**B-C**) Thick-section images and quantification of the association between adrenergic nerves and the prostate vasculature in the low-grade PIN (LPIN) stage. Representative images of wild-type (WT) prostate (top) and LPIN stage prostate (bottom). TH = tyrosine hydroxylase, CD31 = vasculature. Scale bar = 100μm (B). Quantification of LPIN stage vascular density (left), adrenergic nerve density (middle), and proximity of association between nerves and vessels (right). n = 4 mice/condition (C). (**D**) FACS quantification of epithelial cell proliferation during LPIN and HPIN stages. n = 4 mice/condition. *p<0.05. Error bars = s.e.m.

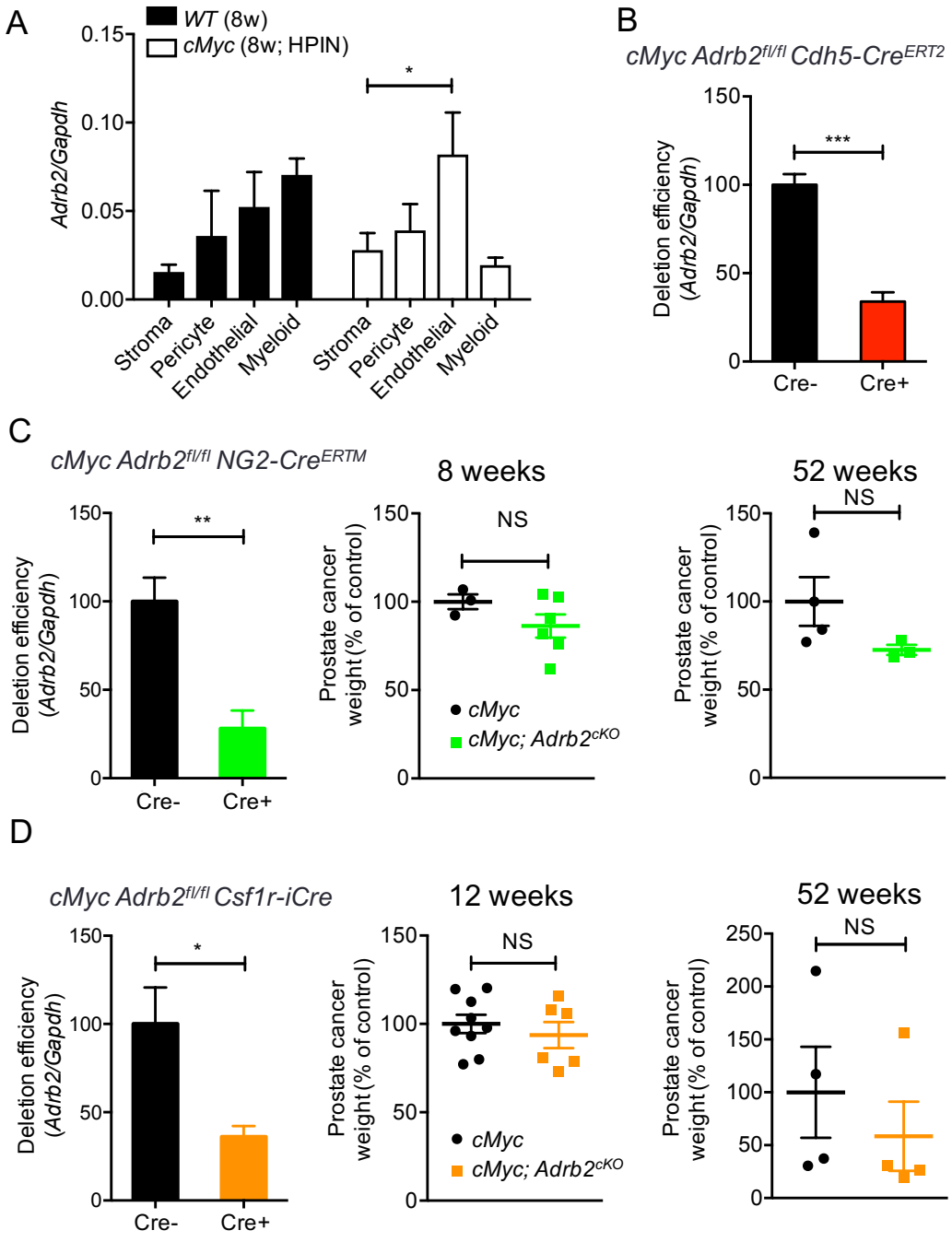

Fig. S3. *Adrb2* is expressed and efficiently deleted in prostate stromal cells, but does not contribute to cancer progression in non-endothelial stromal cells. (**A**) Quantification of *Adrb2* expression in various angiogenesis-associated stromal populations in healthy and HPIN stage prostates isolated by FACS. n = 4 mice/condition. Stroma = $CD45^-$, $CD31^-$, $CD140a^-$, $CD140b^-$, $Epcam^-$ cells. (**B**) *Adrb2* expression in FACS-sorted endothelial cells from HPIN-stage prostates. n = 3 mice/condition. (**C**) *Adrb2* expression in FACS-sorted pericytes from HPIN-stage prostates. n = 4 mice/condition (left), its effect on HPIN-stage cancer progression (middle), and late stage cancer progression (right). (**D**) *Adrb2* expression in FACS sorted myeloid cells from HPIN-stage prostates. n = 4-5 mice/condition (left), its effect on HPIN-stage cancer progression (middle), and late stage cancer progression (right). NS $p>0.05$. *$p<0.05$. **$p<0.01$. ***$p<0.001$. Error bars = s.e.m.

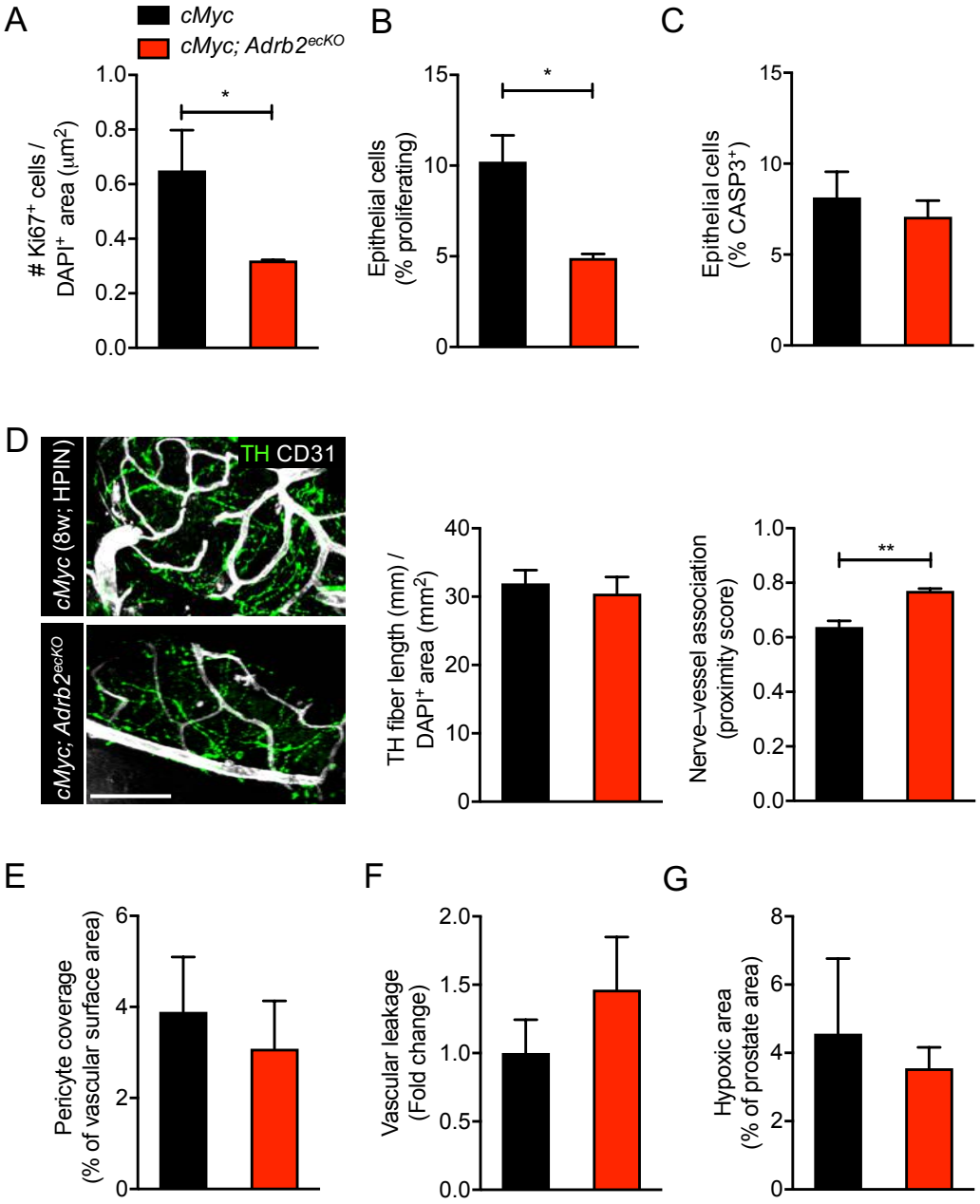

Fig. S4. *Adrb2* deletion in endothelial cells inhibits cancer progression and decreases nerve – vessel interaction. (**A**) Quantification of immunostained Ki-67^{+} proliferative cells in prostate sections n = 3 mice/condition. (**B**) FACS quantification of Ki-67^{+} proliferative epithelial cells n = 6 mice/condition, and (**C**) quantification of cleaved CASP3^{+} apoptotic epithelial cells n = 6 mice/condition. (**D**) Thick-section images of HPIN stage *cMyc* prostate (left, top) and *cMyc; Adrb2^{ecKO}* (left, bottom). TH = tyrosine hydroxylase, CD31 = vasculature. Scale bar = 100μm. Quantification of adrenergic nerve density (middle), and proximity of association between nerves and vessels (right). n = 4 mice/condition. (**E**) Quantification of vascular coverage by pericytes marked by NG2. n = 4 mice/condition. (**F**) Quantification of vascular leakage as assessed by accumulation of IV injected fluorescent dextran in the prostate interstitium. n = 4 mice/condition. (**G**) Tissue hypoxia assessed in prostate cross-sections by pimonidazole positive areas. n = 4 mice/condition. *p<0.05. **p<0.01. Error bars = s.e.m.

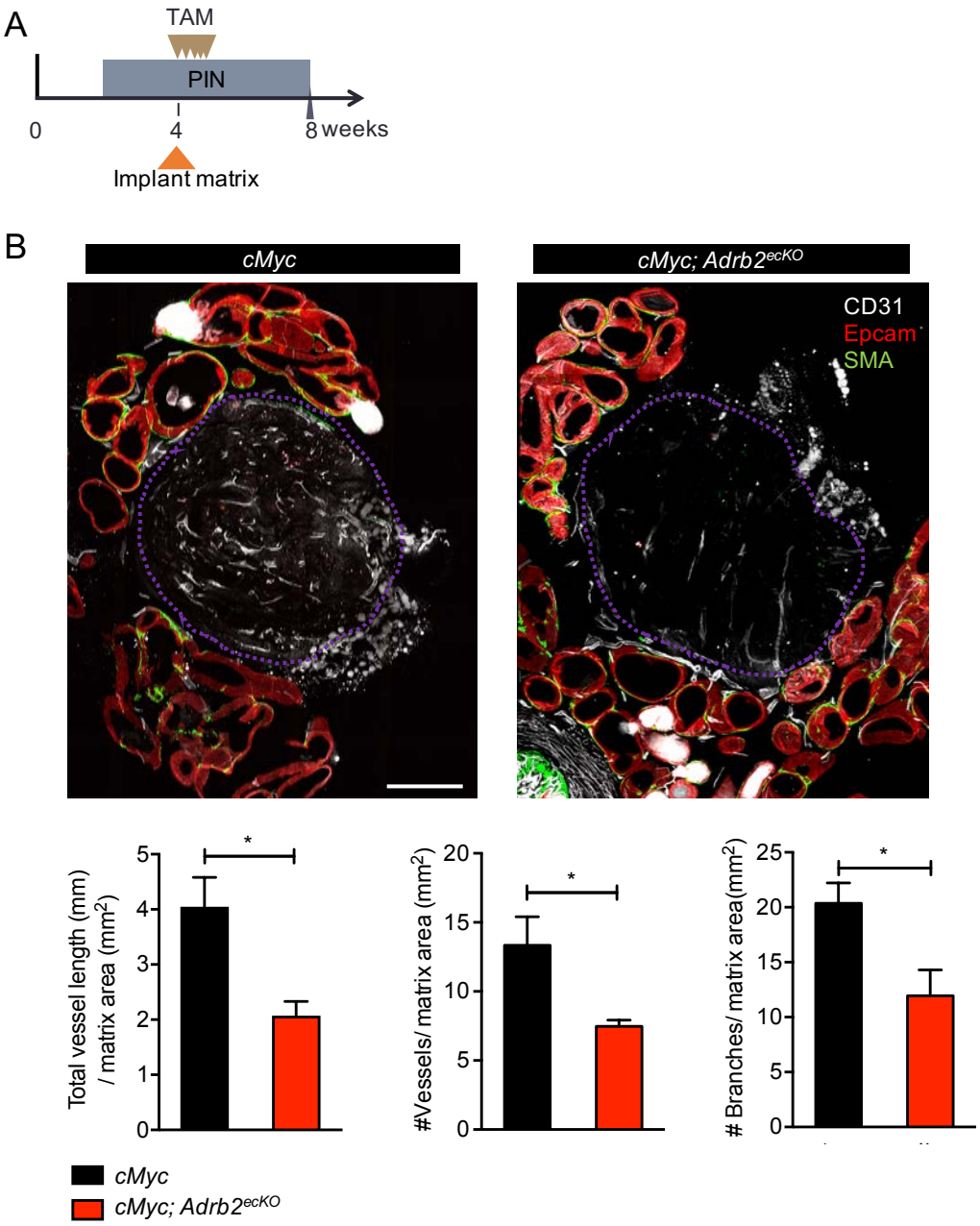

Fig. S5. *Adrb2* deletion in endothelial cells inhibits angiogenesis. (**A**) Experimental design of orthotopic type I collagen matrix vessel migration assay. (**B**) Immunofluorescence analysis of vascular migration into orthotopic matrices (outlined in purple) analyzed at HPIN-stage. Cross-sectional montage of *cMyc* ventral prostate (left, top); Montage of *cMyc; Adrb2*^{ecKO} ventral prostate (right, top). CD31 = vasculature; Epcam = epithelium; SMA = smooth muscle actin. Scale bar = 500μm. Quantification of vessel migration and branching into orthotopic type I collagen matrix after endothelial *Adrb2* deletion (bottom). n = 4 mice/condition. *p<0.05. Error bars = s.e.m.

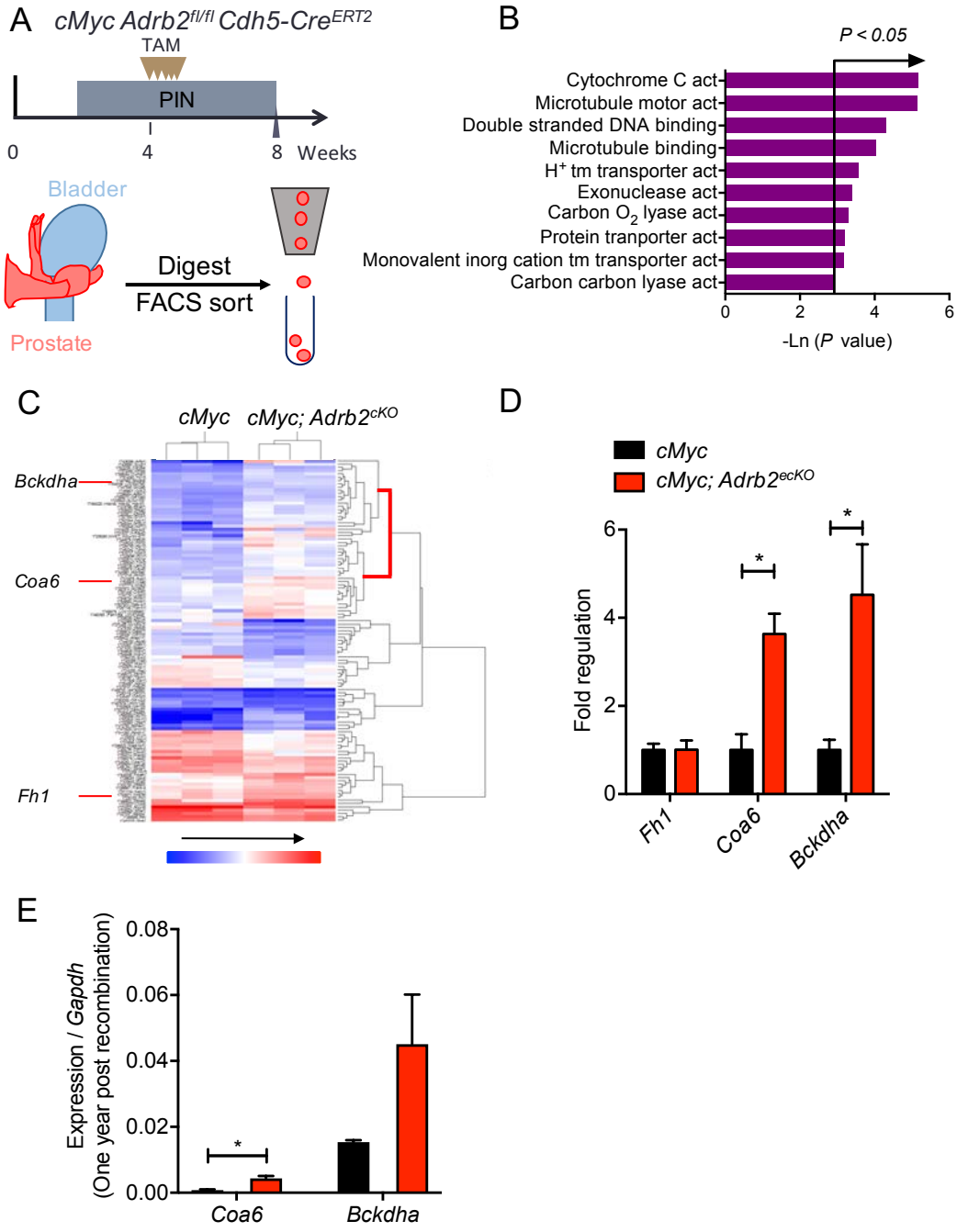

Fig. S6. Transcriptome analysis revealed *Adrb2* deletion increases endothelial oxidative metabolism program in the HPIN-stage and is maintained overtime. (**A-C**) Experimental design and microarray analysis of FACS isolated endothelial cells from *cMyc* and *cMyc; Adrb2*^{ecKO} HPIN-stage prostates. Experimental design (A). Enriched Gene Ontology (GO) terms in *cMyc; Adrb2*^{ecKO} *vs. cMyc* obtained by GSEA (B). Heat map of differentially expressed genes, arranged by unsupervised hierarchical clustering. Upregulated mitochondrial-associated genes that clustered, are highlighted by red bracket. n = 3 mice/condition (C). (**D**) Quantitative PCR validation of *cMyc; Adrb2*^{ecKO} up-regulated metabolic genes. n = 3 mice/condition. (**E**) Expression of the mitochondrial oxidative phosphorylation genes in FACS isolated prostate endothelial cells one year after recombination. n = 3 mice/condition. **p*<0.05. ***p*<0.01. Error bars = s.e.m.

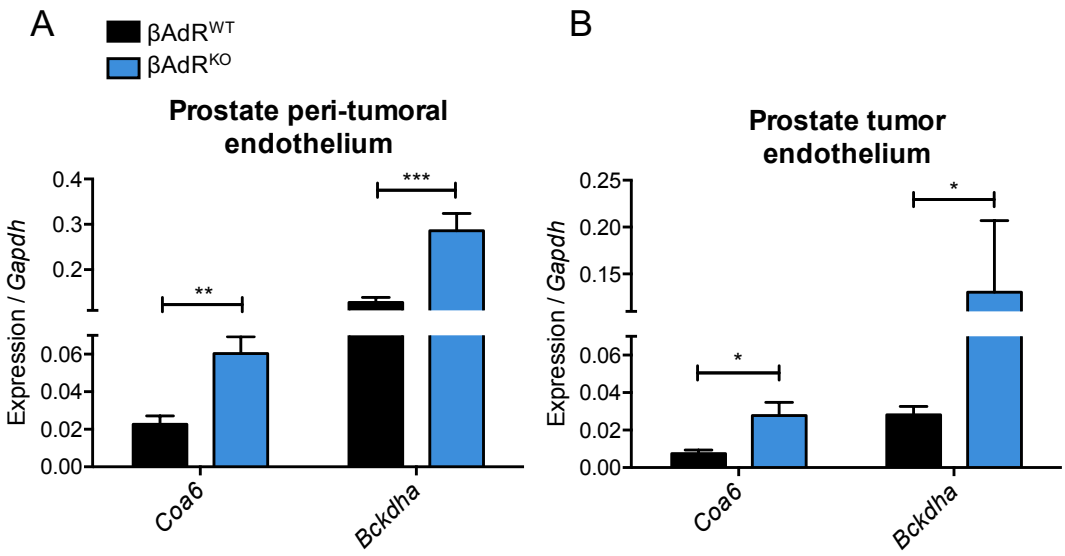

Fig. S7. β-adrenergic receptor deletion in the tumor microenvironment increases expression of mitochondrial metabolism genes in endothelial cells. (**A-B**) Quantitative PCR of mitochondrial metabolism genes in FACS-sorted endothelial cells isolated from βAdR^{WT} and βAdR^{KO} peri-tumoral prostate (A) and from within the orthotopic tumor (B). n = 5 mice/condition. *$p<0.05$. **$p<0.01$. ***$p<0.001$. Error bars = s.e.m.

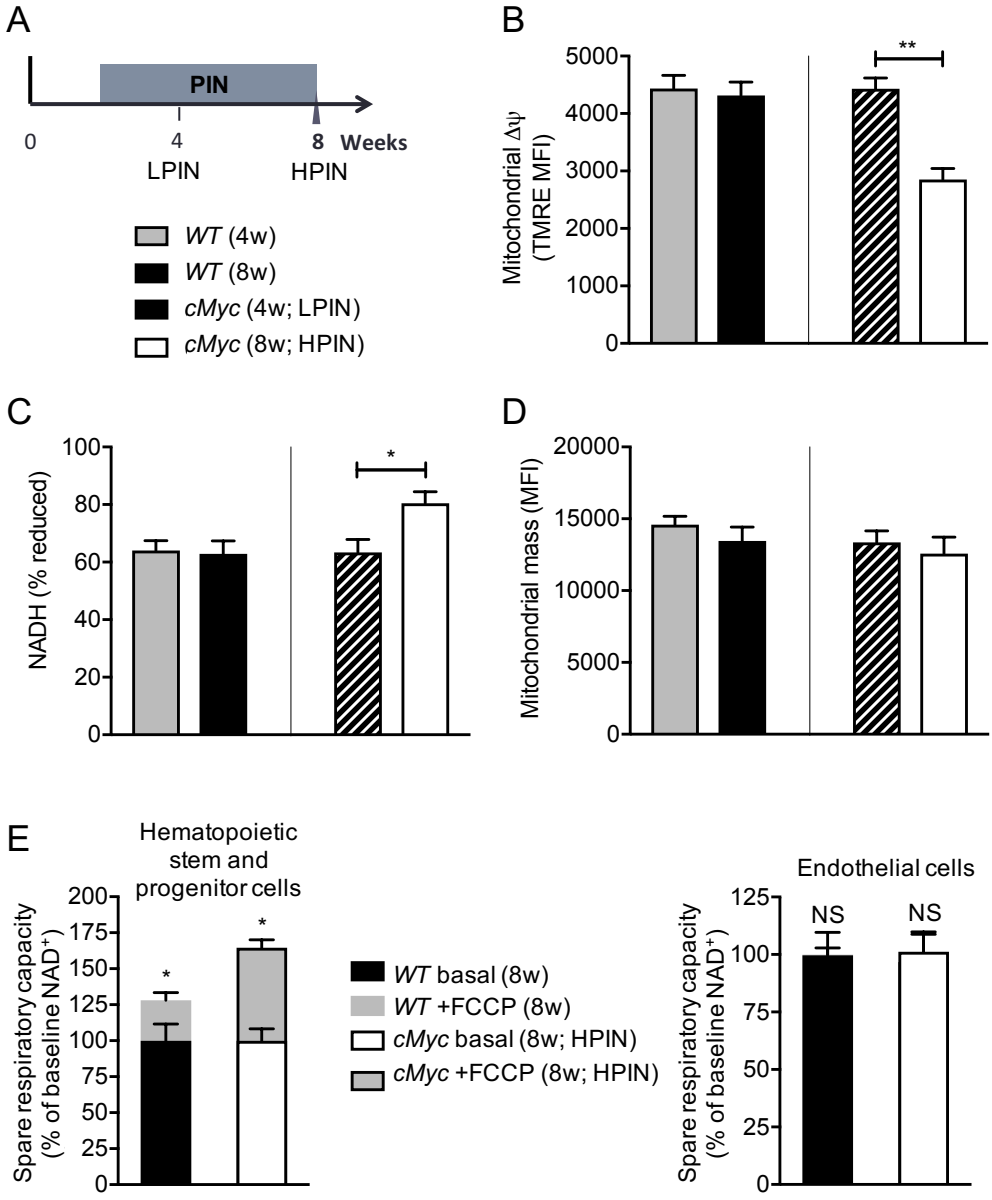

Fig. S8. A metabolic switch occurs during the transition from the pre-neoplastic LPIN to cancer-committed HPIN stage. (**A**) Schematic of disease progression. (**B-D**) FACS analysis of metabolism in freshly isolated prostate endothelial cells. Quantification of Δψ by TMRE staining (B), NADH redox state, the main electron donor in oxidative phosphorylation (C), and mitochondrial mass by Mitotracker green staining (D). n = 4-5 mice/condition. (**E**) Quantification of spare respiratory capacity (SRC) by FACS in freshly isolated bone marrow hematopoietic stem and progenitor cells ($cKit^+$ $Sca\text{-}1^+$ $CD11b^-$ $B220^-$ $CD3^-$ $Gr\text{-}1^-$ $Ter119^-$) as well as prostate endothelial cells isolated from the same animals. n = 4 mice/condition. *p<0.05. **p<0.01. ***p<0.001. Error bars = s.e.m.

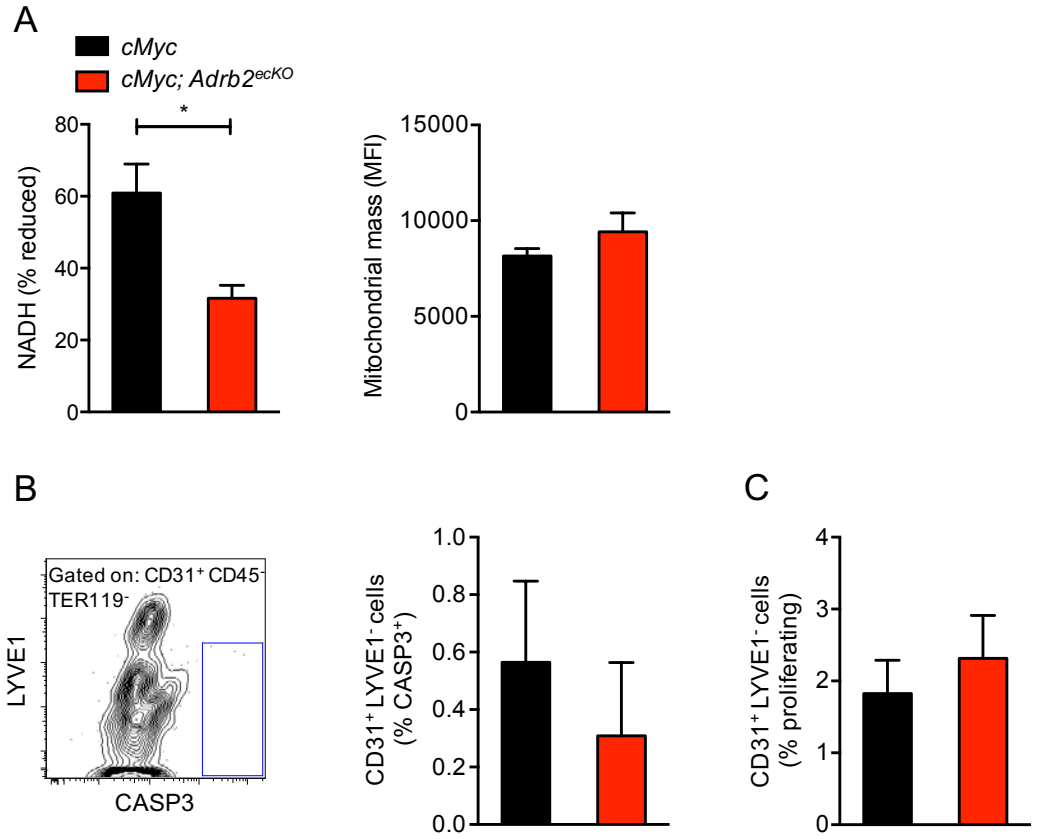

Fig. S9. *Adrb2* deletion does not affect endothelial viability or mitochondrial mass. (**A-C**) FACS analysis of endothelial cells isolated from HPIN-stage prostates. (A) Quantification of NADH redox state (left), n = 6-7 mice/condition; and mitochondrial mass by Mitotracker green staining (right), n = 4-5 mice/condition. (B) Representative cleaved $CASP3^+$ apoptotic endothelial cell plot (left), and quantification (right). n = 7 mice/condition. (C) Quantification of Ki-67^+ proliferative endothelial cells. n = 4 mice/condition. *p<0.05. Error bars = s.e.m.

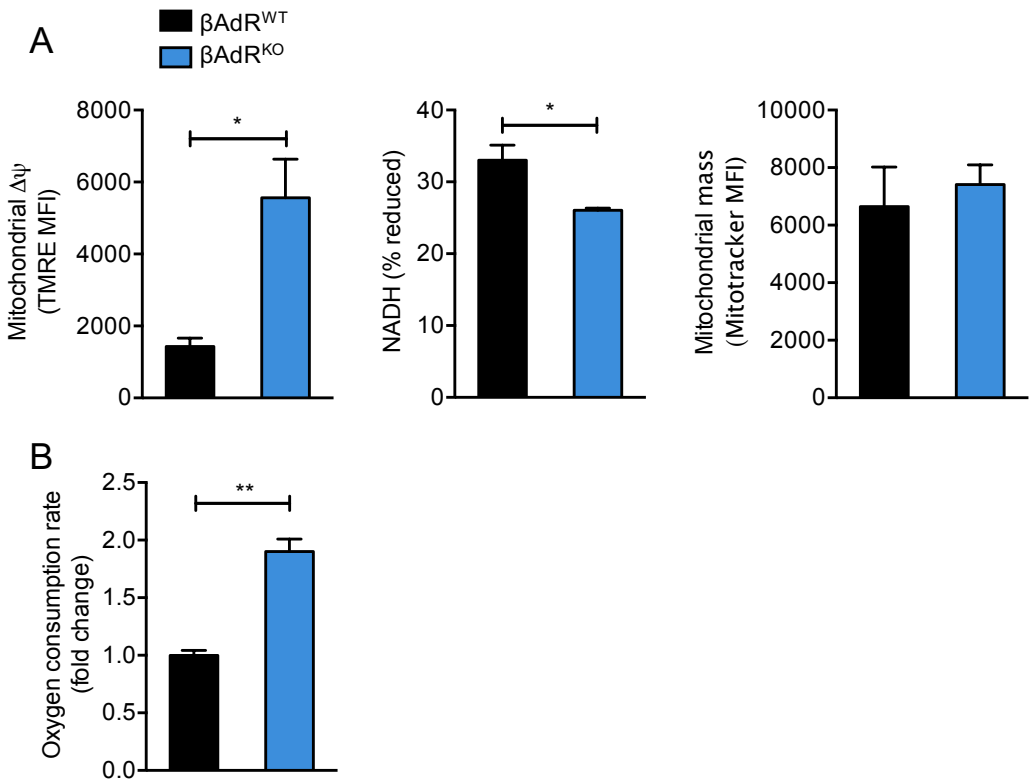

Fig. S10. β-adrenergic receptor deletion in the tumor microenvironment increases endothelial oxidative metabolism. (**A**) FACS analysis of Δψ by TMRE staining (left), NADH redox state (middle), and mitochondrial mass by Mitotracker green staining (right). n = 3 mice/condition. (**B**) Relative oxygen consumption rate in βAdR^{WT} and βAdR^{KO} primary tumor endothelial cells, freshly isolated by FACS sorting and incubated with noradrenaline for 36 h before analysis. n = 3 mice/condition. *p<0.05. **p<0.01. Error bars = s.e.m.

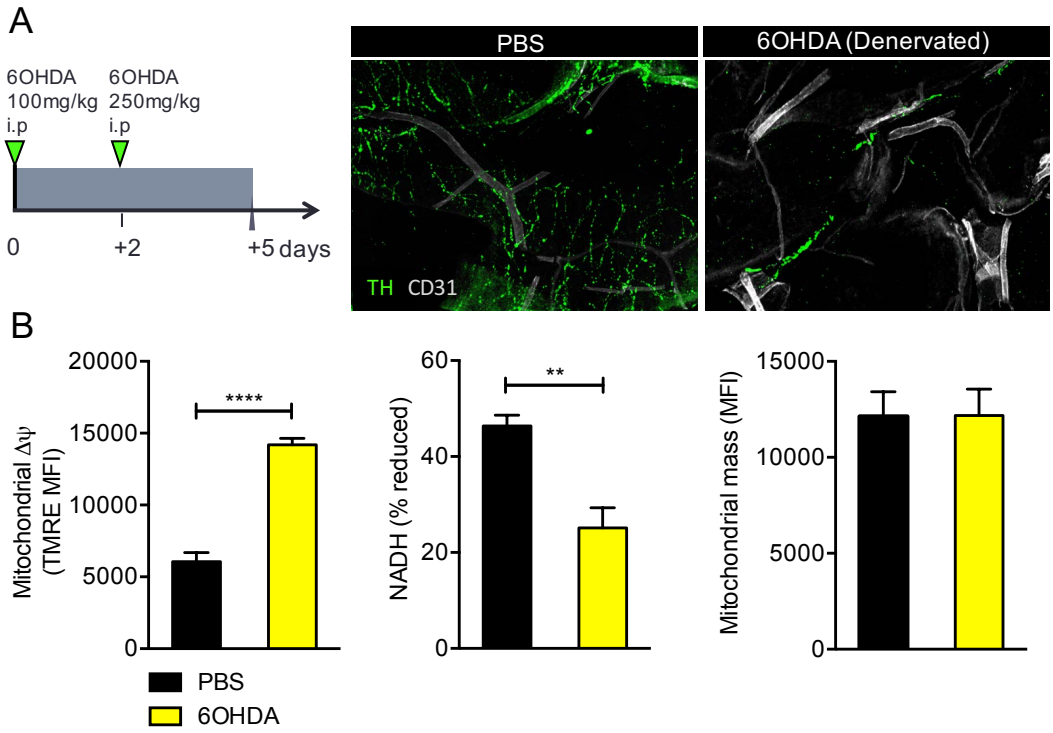

Fig. S11. Adrenergic denervation increases endothelial oxidative metabolism. (**A**) Experimental design (left), and representative images of PBS (middle), and 6OHDA chemically sympathectomized prostates (right). (**B**) FACS analysis of Δψ by TMRE staining (left), NADH redox state (middle), and mitochondrial mass by Mitotracker green staining (right). n = 4 mice/condition. **p<0.01. ****p<0.0001. Error bars = s.e.m.

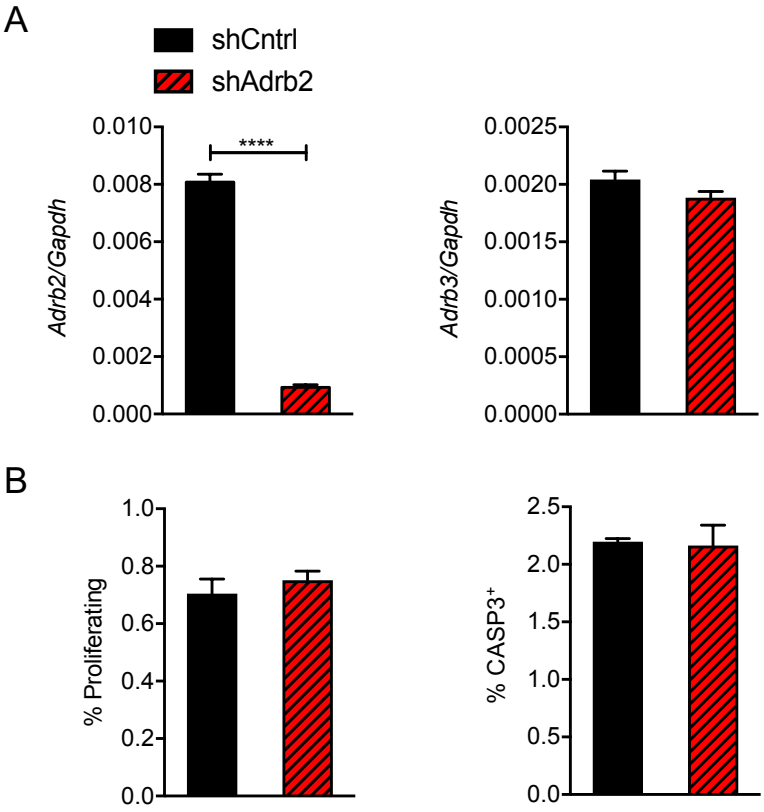

Fig. S12. *Adrb2* knockdown is specific and does not affect cell viability. (**A**) *Adrb2* expression (left) and non-targeted *Adrb3* expression (right) assessed by quantitative PCR. n = 3 independent experiments. (**B**) FACS quantification of cleaved CASP3^{+} apoptotic cells (left) and quantification of Ki-67^{+} proliferative cells (right). n = 3 independent experiments. ****p<0.0001. Error bars = s.e.m.

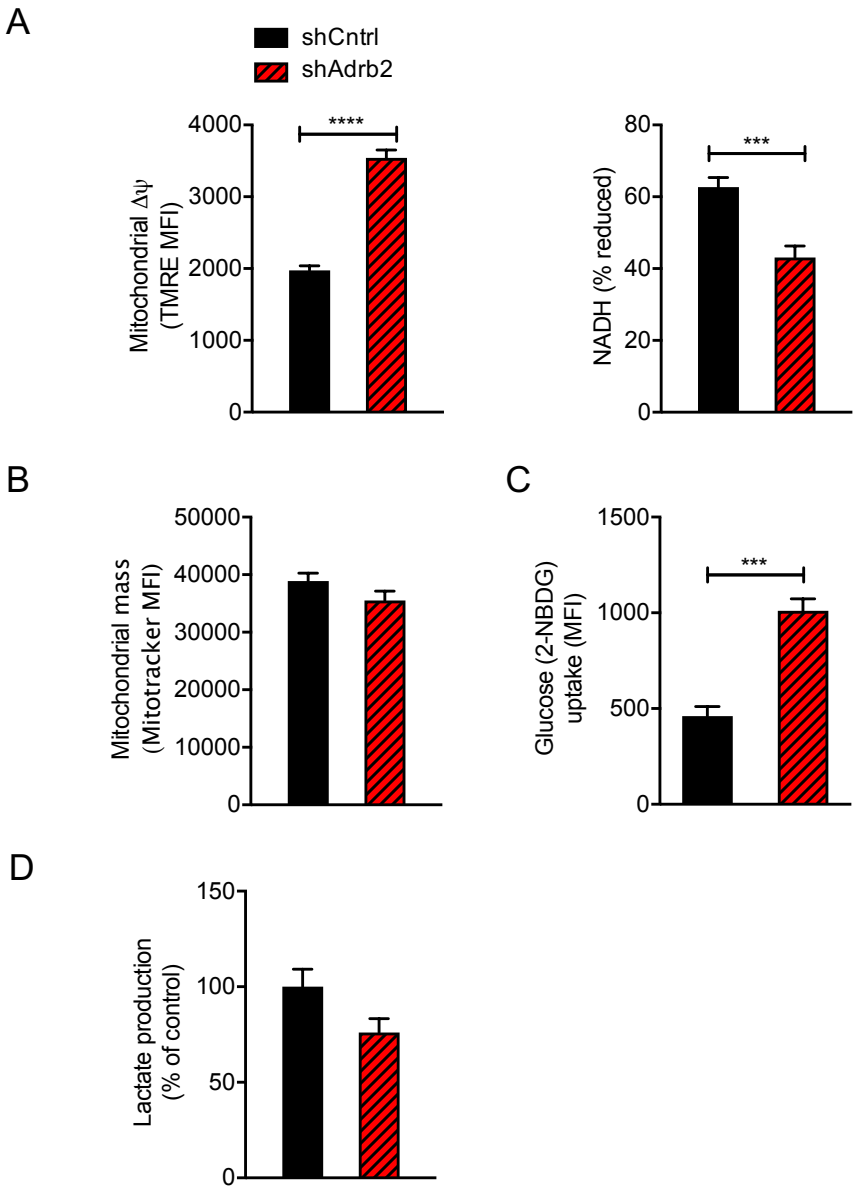

Fig. S13. ***Adrb2*** **knockdown increases oxidative phosphorylation metabolism.** (**A-C**) FACS analysis of endothelial cell metabolism. Quantification of Δψ by TMRE staining (left), and NADH redox state (right) experiments (A). Quantification of mitochondrial mass by Mitotracker green staining (B), and glucose uptake by 2-NBDG (C). n = 3 independent experiments. (**D**) Quantification of extracellular lactate relative to shCntrl. n = 3 independent experiments. ***p<0.001. ****p<0.0001. Error bars = s.e.m.

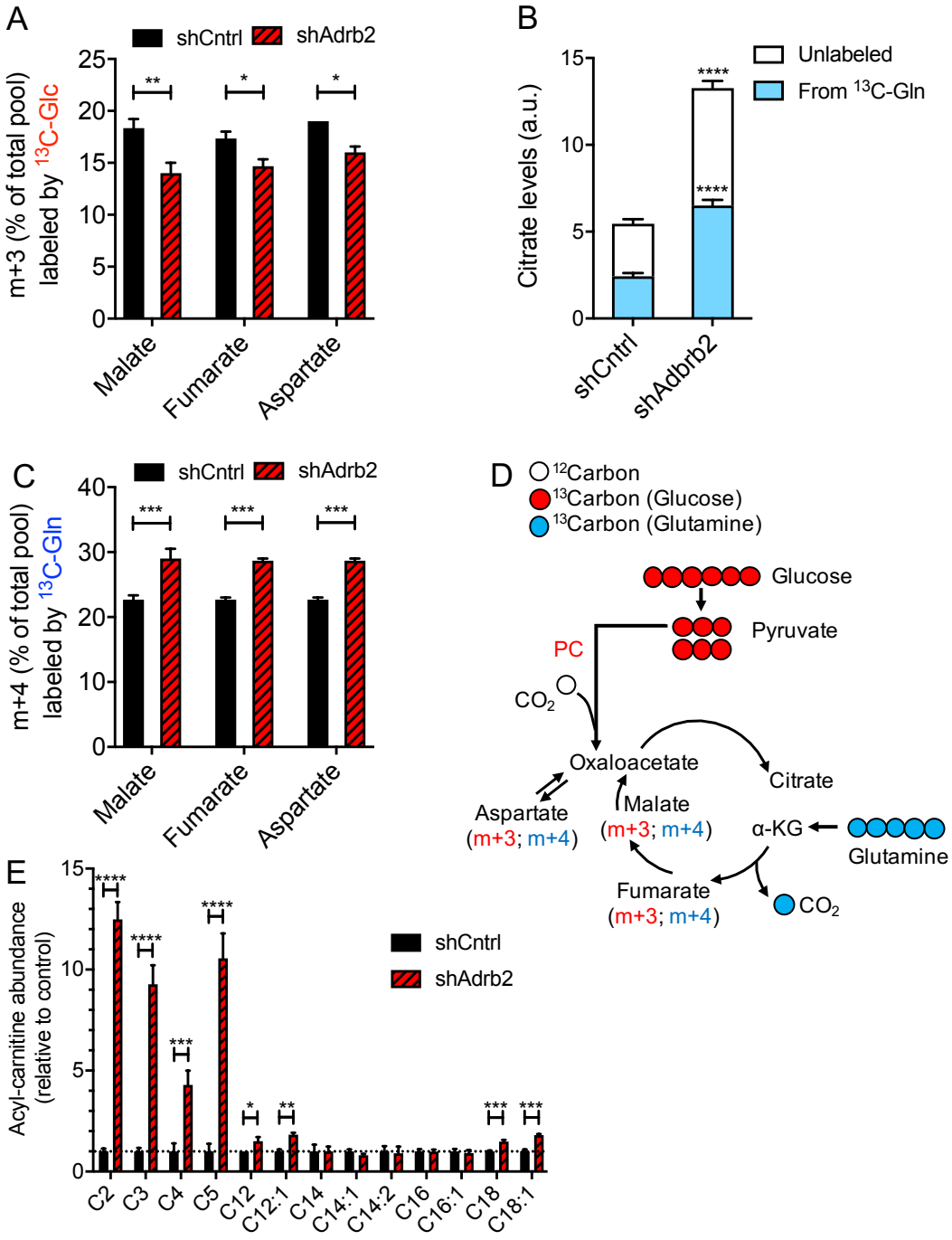

Fig. S14. Characterization of endothelial metabolism after *Adrb2* knockdown. (**A**) Fraction of malate, fumarate, and aspartate containing three ^{13}C-labeled carbons derived from [U-^{13}C]-glucose. n = 3 replicates/ condition. (**B-C**) Panels B-C represent different analyses of the same set of experiments (n = 3 replicates/ condition. Metabolite levels were normalized to internal standard and to sample protein content). Relative intracellular levels of citrate labeling derived from [U-^{13}C]-glutamine (B). Fraction of malate, fumarate, and aspartate containing four ^{13}C-labeled carbons derived from [U-^{13}C]-glutamine (C). (**D**) Schematic describing anaplerotic TCA metabolite labeling pattern derived from [U-^{13}C]-glucose and [U-^{13}C]-glutamine. (**E**) Metabolite profiling of acyl carnitine abundance. Dotted line represents shCntrl metabolite levels. n = 4 replicates/ conditions. *p<0.05. **p<0.01.***p<0.001. ****p<0.0001. Error bars = s.e.m.

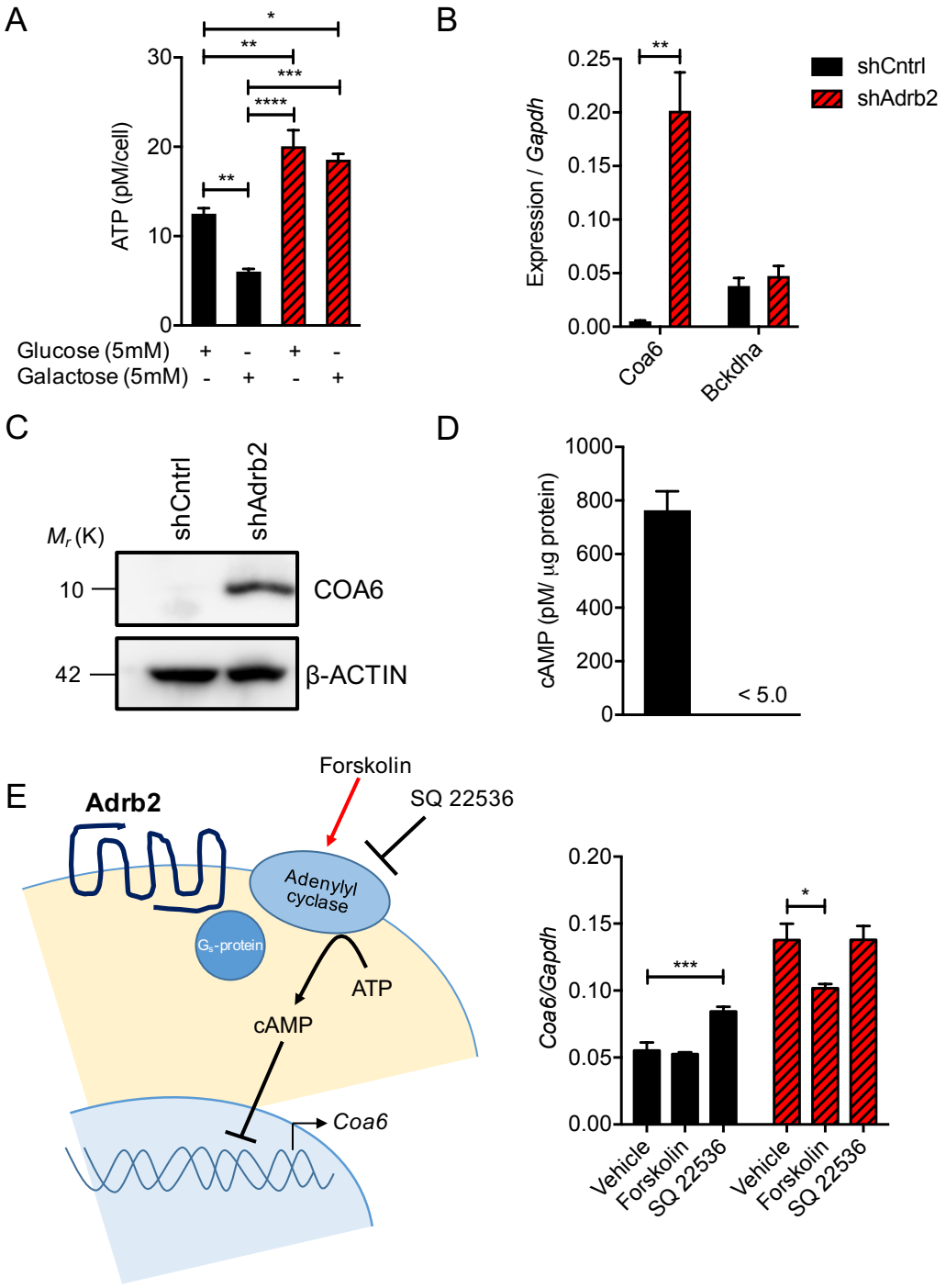

Fig. S15. ADRB2 regulates endothelial *Coa6* expression via cAMP signaling. (**A**) Quantification of ATP levels in cells cultured in the presence of glucose or galactose. n = 3 independent experiments. (**B**) Quantitative PCR of mitochondrial metabolism genes. n = 3 independent experiments. (**C**) Western blot of the mitochondrial metabolism protein COA6. (**D**) Quantification of the second messenger cAMP in the presence of noradrenaline. n = 3 independent experiments. (**E**) The effect of adenylyl cyclase inhibition (by SQ 22536), or stimulation (by forskolin), on *Coa6* expression in the presence of noradrenaline. Schematic of signaling pathway (left), and quantification of expression by quantitative PCR (right). **p*<0.05. ***p*<0.01. ****p*<0.001. *****p*<0.0001. Error bars = s.e.m.

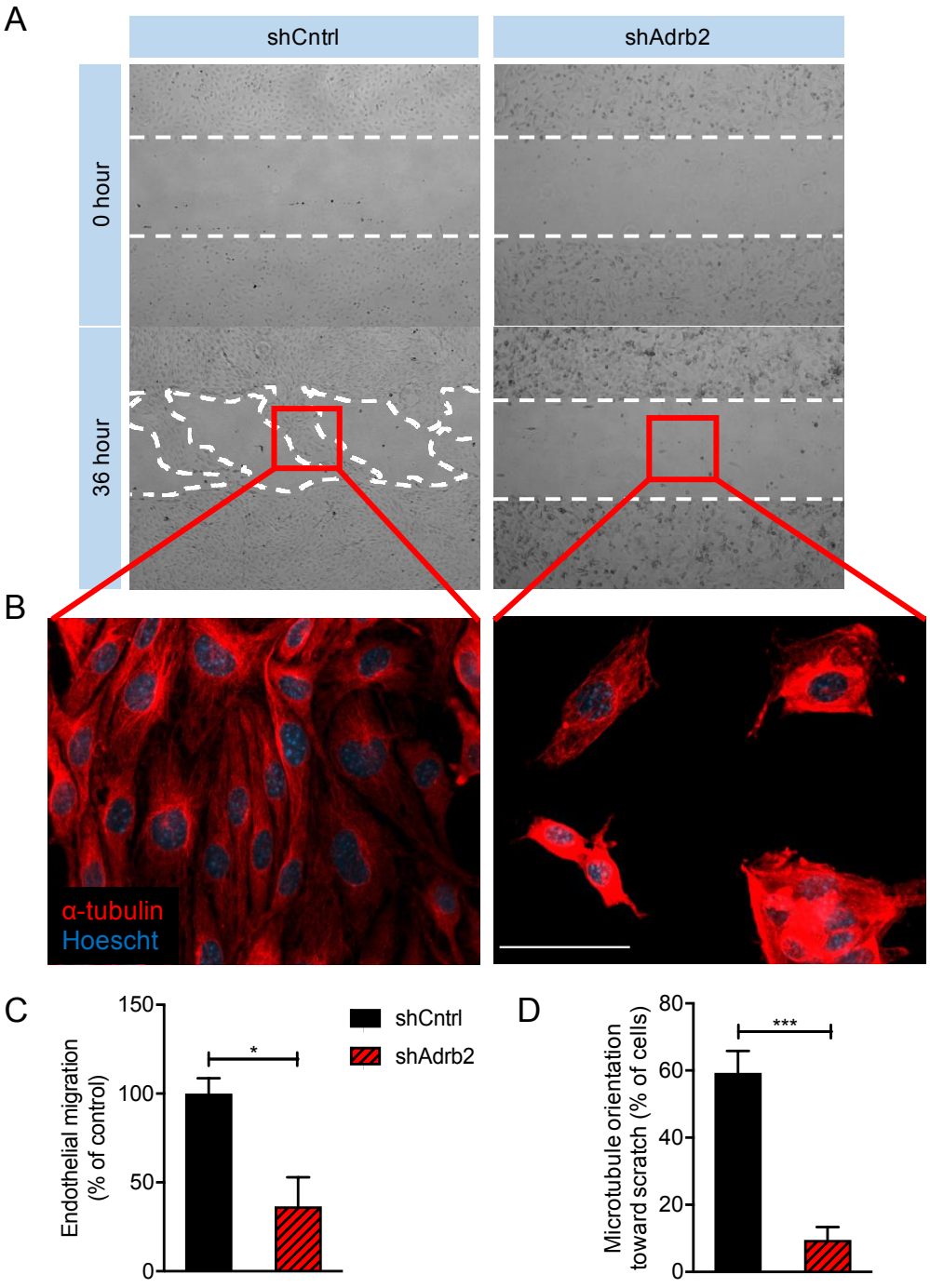

Fig. S16. ***Adrb2*** **knockdown inhibits endothelial cell migration.** (**A-D**) Endothelial migration and microtubule organization in a scratch wound assay. Representative images of shCntrl and shAdrb2 at 0 hours after the scratch was made (top) and 36 hours later (bottom) (A). Immunofluorescent images of microtubule orientation in cells that migrated into the scratch. Scale bar = 50µm. (B). Quantification of endothelial migration (left) and microtubule orientation (right). n = 3 independent experiments. *p<0.05. ***p<0.001. Error bars = s.e.m.

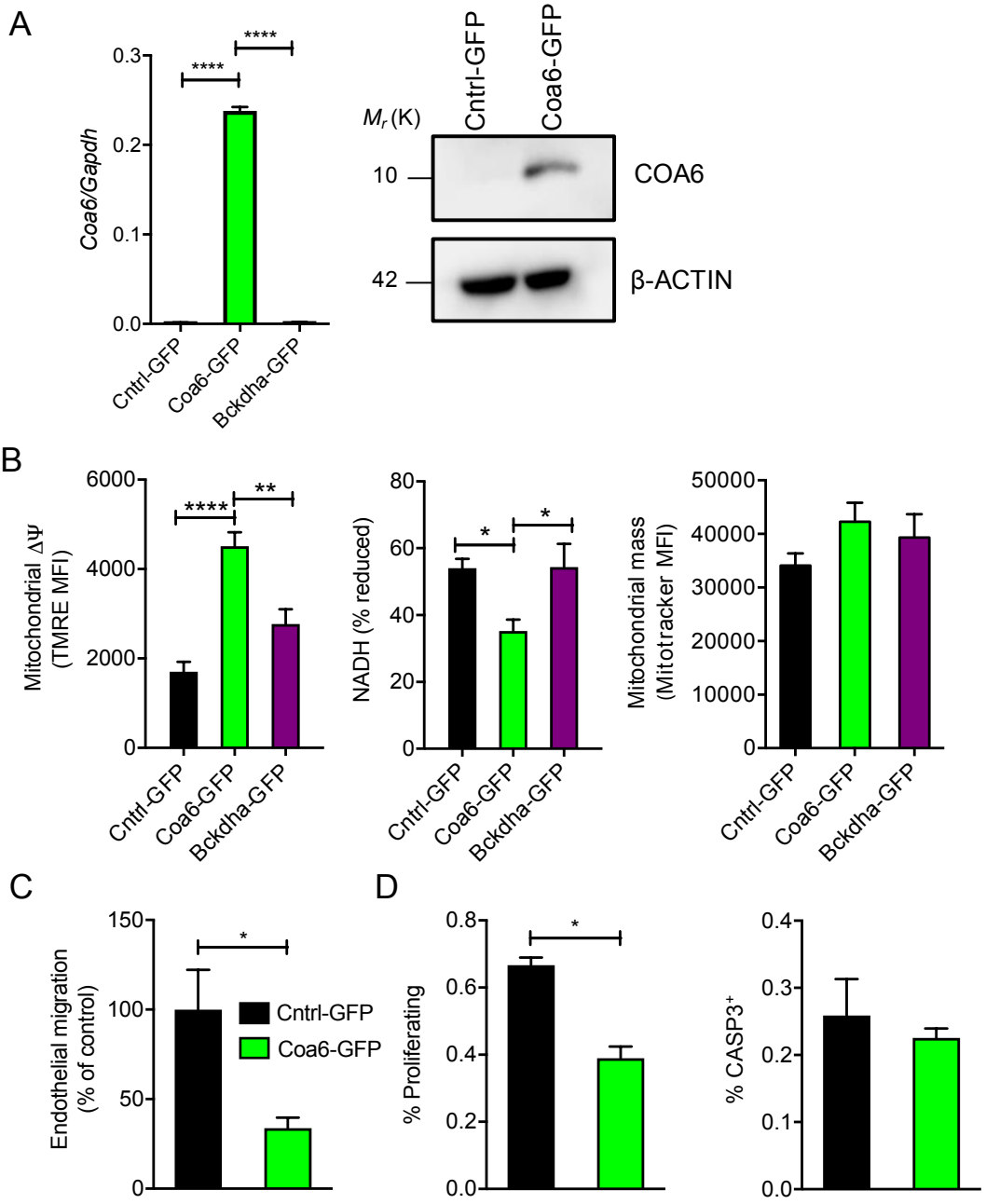

Fig. S17. *Coa6* expression increases endothelial oxidative phosphorylation. (**A**) Validation that *Coa6* overexpression (Coa6-GFP) in primary prostate endothelial cells increases both *Coa6* mRNA expression by quantitative PCR (left) and COA6 protein levels by western blot (right). (**B**) FACS analysis of of Δψ by TMRE staining (left), NADH redox state (middle), and mitochondrial mass (right). n = 3 independent experiments. (**C**) Quantification of endothelial cell migration in a scratch wound assay. n = 3 independent experiments. (**D**) FACS quantification of Ki-67^{+} proliferating endothelial cells (left) and cleaved CASP3^{+} apoptotic cells (right). n = 3 independent experiments. *p<0.05. **p<0.01. ****p<0.0001. Error bars = s.e.m.

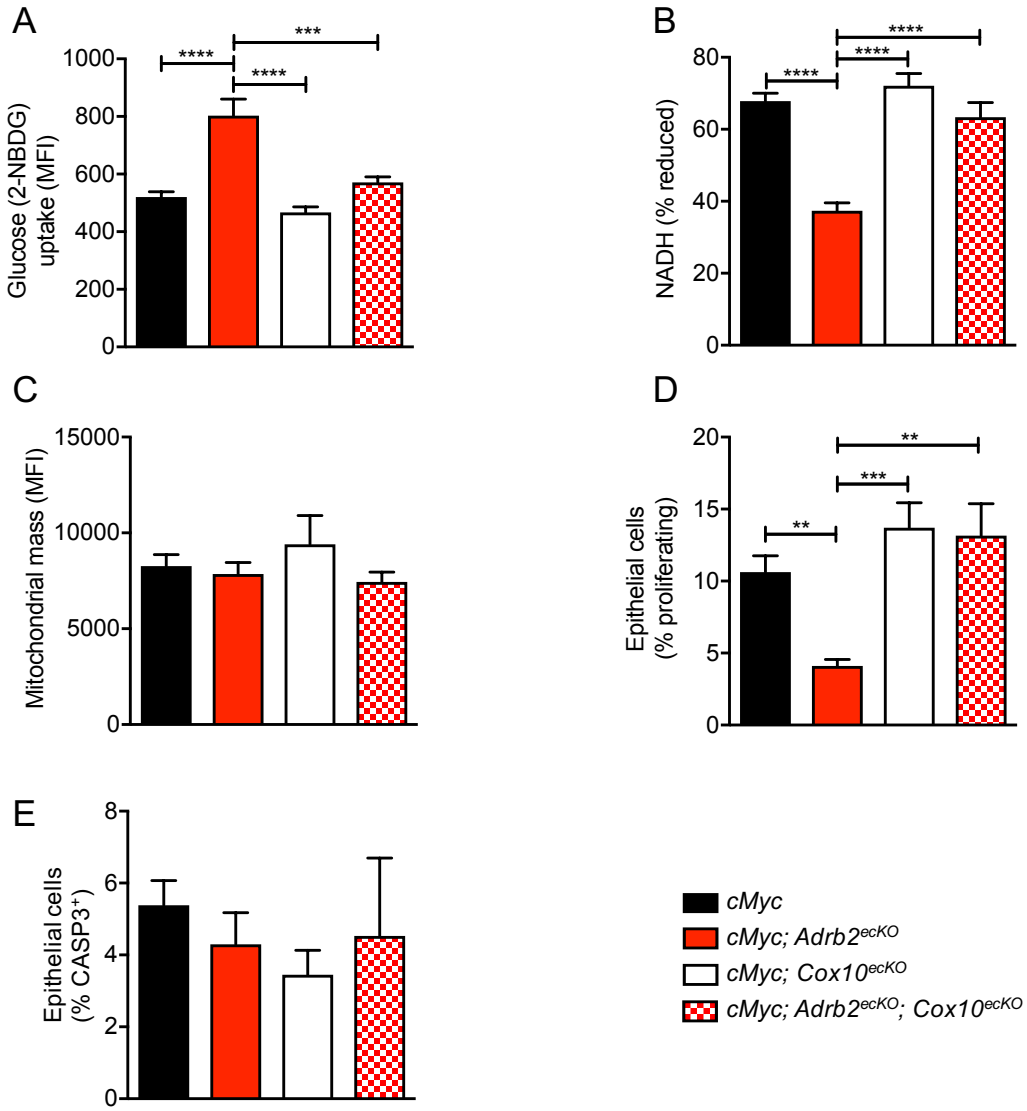

Fig. S18. *Cox10* co-deletion restores endothelial metabolism and cancer progression. (**A-E**) HPIN-stage analysis of *cMyc*, *cMyc; Adrb2*^{ecKO}, *cMyc; Cox10*^{ecKO}, and double *cMyc; Adrb2*^{ecKO}*; Cox10*^{ecKO} showing that deletion of both *Adrb2* and *Cox10* restores glucose uptake (A; n = 6-7 mice/condition), and NADH redox ratio (B; n = 6-7 mice/condition), without affecting mitochondrial mass (C; 6-7 mice/condition), and restores epithelial proliferation (D; n = 6-7 mice/condition), without affecting apoptosis (E; n = 6-7 mice/condition). *p<0.05. **p<0.01. ***p<0.001. ****p<0.0001. Error bars = s.e.m.

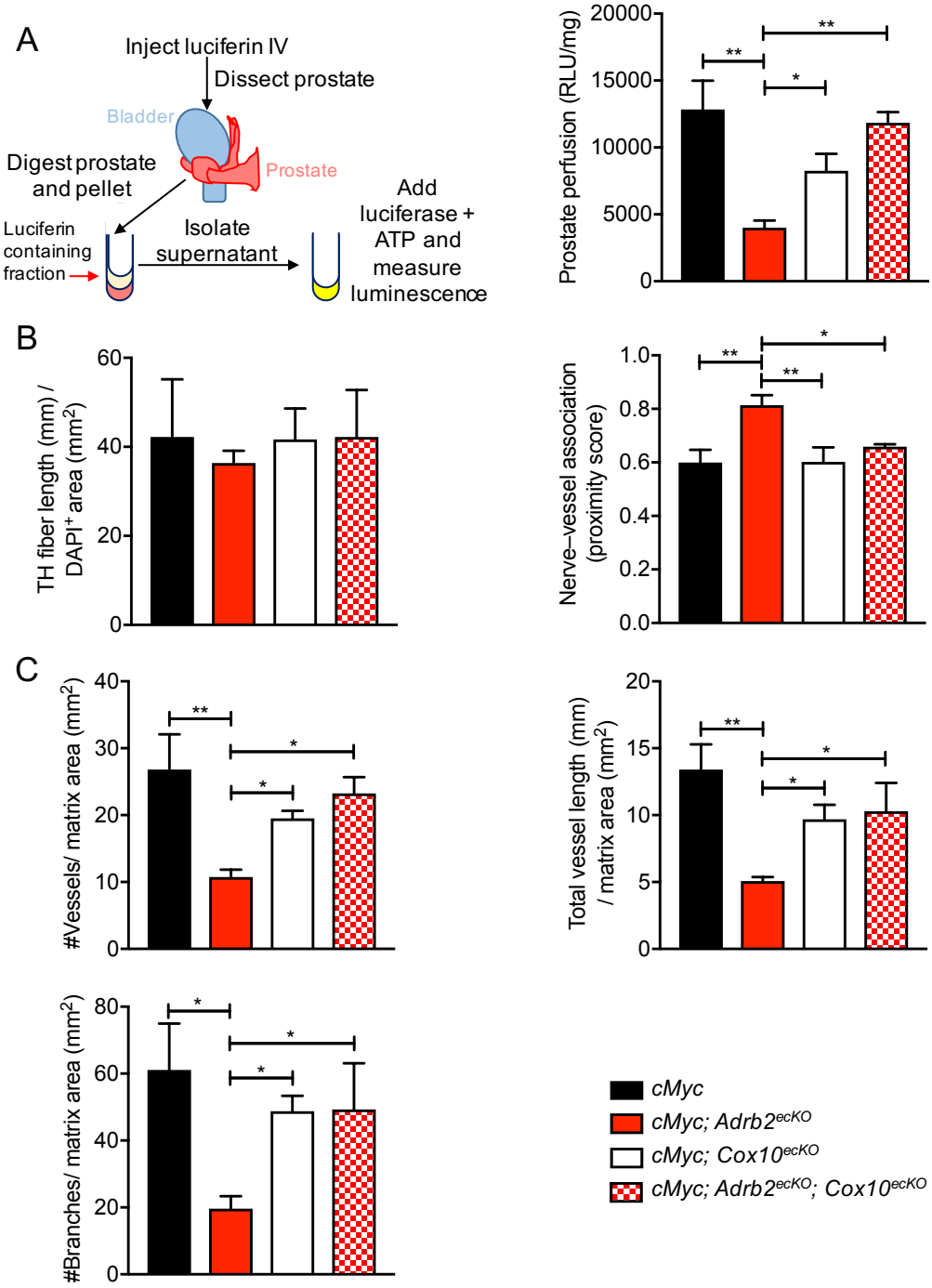

Fig. S19. ***Cox10*** **co-deletion restores prostate perfusion and angiogenesis.** (**A**) Schematic summarizing luciferin-based prostate perfusion assay (left) and quantification of prostate perfusion (right). n = 4 mice/condition. (**B**) Quantification of adrenergic nerve density (left), and proximity of association between nerves and vessels (right). n = 4 mice/condition. (**C**) Quantification of vessel migration, density, and branching into orthotopic type I collagen matrices after endothelial *Adrb2, Cox10,* or *Adrb2* + *Cox10* deletion. n = 4 mice/condition. **p*<0.05. ***p*<0.01. Error bars = s.e.m.

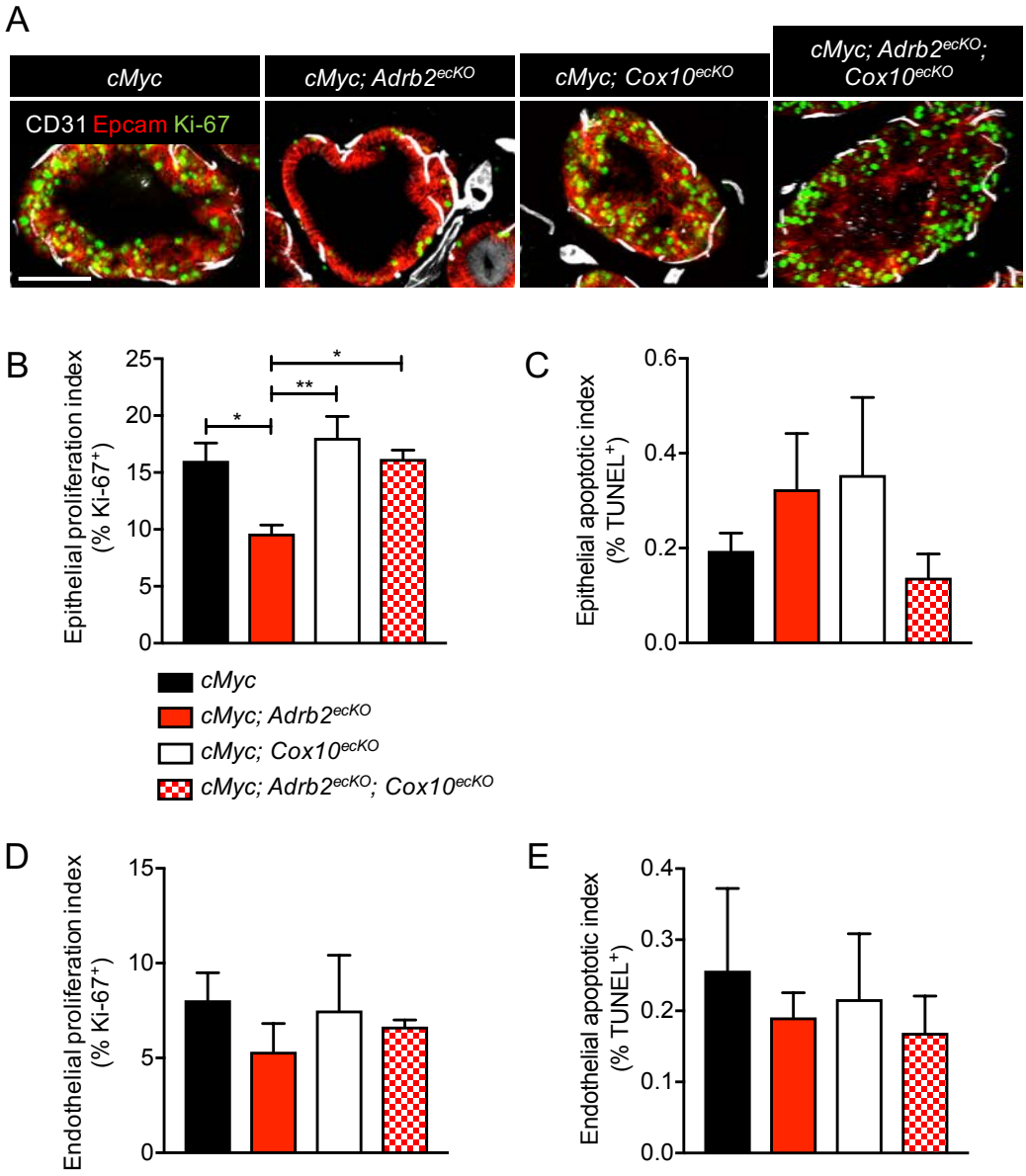

Fig. S20. ***Cox10*** **co-deletion restores epithelial proliferation, but does not affect endothelial proliferation or viability.** (**A-E**) Immunofluorescence analysis of epithelial and endothelial proliferation and apoptosis. Thin cross-sectional images of *cMyc*, *cMyc; Adrb2*^{ecKO}, *cMyc; Cox10*^{ecKO}, and *cMyc; Adrb2*^{ecKO}*; Cox10*^{ecKO} prostates. Scale bar = 100μm (A). Quantification of Ki-67^{+} proliferating epithelial cells (B), TUNEL^{+} apoptotic epithelial cells (C), Ki67^{+} proliferating endothelial cells (D), and TUNEL^{+} apoptotic endothelial cells (E). **p*<0.05. ***p*<0.01. Error bars = s.e.m.

Table S1. Isotopologue distribution of citrate derived from [U-^{13}C]-glutamine

	Fraction labeled by ^{13}C-Gln		
Isotopologue of Citrate	**shCntrl** ***n*** **= 3**	**shAdrb2** ***n*** **= 3**	**p-value**
m+0	0.55	0.51	<0.0001
m+1	0.11	0.09	<0.0001
m+2	0.11	0.10	0.0004
m+3	0.04	0.07	<0.0001
m+4	0.14	0.16	<0.0001
m+5	0.02	0.07	<0.0001
m+6	0.01	0.00	0.0097

REFERENCES

1. J. Folkman, K. Watson, D. Ingber, D. Hanahan, Induction of angiogenesis during the transition from hyperplasia to neoplasia. *Nature* **339**, 58-61 (1989).
2. G. Bergers, L. E. Benjamin, Tumorigenesis and the angiogenic switch. *Nature reviews. Cancer* **3**, 401-410 (2003).
3. Y. S. Mukouyama, D. Shin, S. Britsch, M. Taniguchi, D. J. Anderson, Sensory nerves determine the pattern of arterial differentiation and blood vessel branching in the skin. *Cell* **109**, 693-705 (2002).
4. W. Li *et al.*, Peripheral nerve-derived CXCL12 and VEGF-A regulate the patterning of arterial vessel branching in developing limb skin. *Dev Cell* **24**, 359-371 (2013).
5. A. J. Ekstrand *et al.*, Deletion of neuropeptide Y (NPY) 2 receptor in mice results in blockage of NPY-induced angiogenesis and delayed wound healing. *Proc Natl Acad Sci U S A* **100**, 6033-6038 (2003).
6. P. Martin, Wound Healing--Aiming for Perfect Skin Regeneration. *Science* **276**, 75-81 (1997).
7. S. W. Cole, A. S. Nagaraja, S. K. Lutgendorf, P. A. Green, A. K. Sood, Sympathetic nervous system regulation of the tumour microenvironment. *Nature reviews. Cancer* **15**, 563-572 (2015).
8. D. He *et al.*, Biologic effect of neurogenesis in pancreatic cancer. *Hum Pathol* **52**, 182-189 (2016).
9. C. Magnon *et al.*, Autonomic nerve development contributes to prostate cancer progression. *Science* **341**, 1236361 (2013).
10. J. L. Saloman *et al.*, Ablation of sensory neurons in a genetic model of pancreatic ductal adenocarcinoma slows initiation and progression of cancer. *Proc Natl Acad Sci U S A* **113**, 3078-3083 (2016).
11. C. M. Zhao *et al.*, Denervation suppresses gastric tumorigenesis. *Science translational medicine* **6**, 250ra115 (2014).
12. M. H. Longair, D. A. Baker, J. D. Armstrong, Simple Neurite Tracer: open source software for reconstruction, visualization and analysis of neuronal processes. *Bioinformatics (Oxford, England)* **27**, 2453-2454 (2011).
13. T. Twardowski, A. Fertala, J. Orgel, J. San Antonio, Type I Collagen and Collagen Mimetics as Angiogenesis Promoting Superpolymers. *Current Pharmaceutical Design* **13**, 3608-3621 (2007).
14. J. A. Tuxhorn *et al.*, Reactive stroma in human prostate cancer: induction of myofibroblast phenotype and extracellular matrix remodeling. *Clin Cancer Res* **8**, 2912-2923 (2002).
15. N. Burns-Cox, N. C. Avery, J. C. Gingell, A. J. Bailey, Changes in Collagen Metabolism in Prostate Cancer: A Host Response That May Alter Progression. *The Journal of Urology* **166**, 1698-1701 (2001).
16. W. J. Huss, C. F. Hanrahan, R. J. Barrios, J. W. Simons, N. M. Greenberg, Angiogenesis and prostate cancer: identification of a molecular progression switch. *Cancer Res* **61**, 2736-2743 (2001).
17. K. Ellwood-Yen *et al.*, Myc-driven murine prostate cancer shares molecular features with human prostate tumors. *Cancer cell* **4**, 223-238 (2003).
18. M. Ittmann *et al.*, Animal models of human prostate cancer: the consensus report of the New York meeting of the Mouse Models of Human Cancers Consortium Prostate Pathology Committee. *Cancer Res* **73**, 2718-2736 (2013).
19. T. Iwata *et al.*, MYC overexpression induces prostatic intraepithelial neoplasia and loss of Nkx3.1 in mouse luminal epithelial cells. *PLoS One* **5**, e9427 (2010).
20. P. Carmeliet, R. K. Jain, Molecular mechanisms and clinical applications of angiogenesis. *Nature* **473**, 298-307 (2011).

21. E. Hinoi *et al.*, The sympathetic tone mediates leptin's inhibition of insulin secretion by modulating osteocalcin bioactivity. *The Journal of cell biology* **183**, 1235-1242 (2008).
22. L. Deng *et al.*, A novel mouse model of inflammatory bowel disease links mammalian target of rapamycin-dependent hyperproliferation of colonic epithelium to inflammation-associated tumorigenesis. *Am J Pathol* **176**, 952-967 (2010).
23. X. Zhu *et al.*, Age-dependent fate and lineage restriction of single NG2 cells. *Development* **138**, 745-753 (2011).
24. I. Sorensen, R. H. Adams, A. Gossler, DLL1-mediated Notch activation regulates endothelial identity in mouse fetal arteries. *Blood* **113**, 5680-5688 (2009).
25. K. De Bock *et al.*, Role of PFKFB3-driven glycolysis in vessel sprouting. *Cell* **154**, 651-663 (2013).
26. K. Wilhelm *et al.*, FOXO1 couples metabolic activity and growth state in the vascular endothelium. *Nature* **529**, 216-220 (2016).
27. Y. H. Wang *et al.*, Cell-state-specific metabolic dependency in hematopoiesis and leukemogenesis. *Cell* **158**, 1309-1323 (2014).
28. F. Kocabas, J. Zheng, C. Zhang, H. A. Sadek, Metabolic characterization of hematopoietic stem cells. *Methods Mol Biol* **1185**, 155-164 (2014).
29. M. Maryanovich *et al.*, An MTCH2 pathway repressing mitochondria metabolism regulates haematopoietic stem cell fate. *Nat Commun* **6**, 7901 (2015).
30. A. Krutzfeldt, R. Spahr, S. Mertens, B. Siegmund, H. M. Piper, Metabolism of exogenous substrates by coronary endothelial cells in culture. *J Mol Cell Cardiol* **22**, 1393-1404 (1990).
31. M. Seandel *et al.*, Generation of a functional and durable vascular niche by the adenoviral E4ORF1 gene. *Proc Natl Acad Sci U S A* **105**, 19288-19293 (2008).
32. T. L. Cheng *et al.*, Pyruvate carboxylase is required for glutamine-independent growth of tumor cells. *Proceedings of the National Academy of Sciences of the United States of America* **108**, 8674-8679 (2011).
33. J. Munger *et al.*, Systems-level metabolic flux profiling identifies fatty acid synthesis as a target for antiviral therapy. *Nature biotechnology* **26**, 1179-1186 (2008).
34. K. A. Hotchkiss *et al.*, Inhibition of endothelial cell function in vitro and angiogenesis in vivo by docetaxel (Taxotere): association with impaired repositioning of the microtubule organizing center. *Molecular cancer therapeutics* **1**, 1191-1200 (2002).
35. R. Suzuki, K. Hotta, K. Oka, Spatiotemporal quantification of subcellular ATP levels in a single HeLa cell during changes in morphology. *Scientific reports* **5**, 16874 (2015).
36. A. Ghosh *et al.*, Copper supplementation restores cytochrome c oxidase assembly defect in a mitochondrial disease model of COA6 deficiency. *Hum Mol Genet* **23**, 3596-3606 (2014).
37. F. Diaz, C. K. Thomas, S. Garcia, D. Hernandez, C. T. Moraes, Mice lacking COX10 in skeletal muscle recapitulate the phenotype of progressive mitochondrial myopathies associated with cytochrome c oxidase deficiency. *Hum Mol Genet* **14**, 2737-2748 (2005).
38. M. Potente, P. Carmeliet, The Link Between Angiogenesis and Endothelial Metabolism. *Annu Rev Physiol* **79**, 43-66 (2017).
39. S. Liu, Y. Soong, S. V. Seshan, H. H. Szeto, Novel cardiolipin therapeutic protects endothelial mitochondria during renal ischemia and mitigates microvascular rarefaction, inflammation, and fibrosis. *Am J Physiol Renal Physiol* **306**, F970-980 (2014).
40. S. Schoors *et al.*, Partial and transient reduction of glycolysis by PFKFB3 blockade reduces pathological angiogenesis. *Cell Metab* **19**, 37-48 (2014).
41. A. Eichmann, I. Brunet, Arterial innervation in development and disease. *Science translational medicine* **6**, 252ps259 (2014).

42. J. B. Aragon-Ching, R. A. Madan, W. L. Dahut, Angiogenesis inhibition in prostate cancer: current uses and future promises. *Journal of oncology* **2010**, 361836 (2010).
43. G. Bergers, D. Hanahan, Modes of resistance to anti-angiogenic therapy. *Nature reviews. Cancer* **8**, 592-603 (2008).
44. J. Kohl, A. D. Ostrovsky, S. Frechter, G. S. Jefferis, A bidirectional circuit switch reroutes pheromone signals in male and female brains. *Cell* **155**, 1610-1623 (2013).
45. M. Costa, J. D. Manton, A. D. Ostrovsky, S. Prohaska, G. S. Jefferis, NBLAST: Rapid, Sensitive Comparison of Neuronal Structure and Construction of Neuron Family Databases. *Neuron* **91**, 293-311 (2016).
46. B. W. Carey, L. W. Finley, J. R. Cross, C. D. Allis, C. B. Thompson, Intracellular alpha-ketoglutarate maintains the pluripotency of embryonic stem cells. *Nature* **518**, 413-416 (2015).
47. T. Kind *et al.*, FiehnLib: mass spectral and retention index libraries for metabolomics based on quadrupole and time-of-flight gas chromatography/mass spectrometry. *Analytical chemistry* **81**, 10038-10048 (2009).
48. P. Millard, F. Letisse, S. Sokol, J. C. Portais, IsoCor: correcting MS data in isotope labeling experiments. *Bioinformatics (Oxford, England)* **28**, 1294-1296 (2012).